Mineralogical Magazine (2026), 1–22
doi:10.1180/mgm.2025.10188

CAMBRIDGE UNIVERSITY PRESS

Article

Quantifying the P–T conditions of silica enrichment in Archaean cratonic spinel-facies peridotites

Bakang J. Kaekane[1], Emma L. Tomlinson[1] and Brendan C. Hoare[2]

[1]Department of Geology, Trinity College Dublin, Dublin, Ireland; and [2]National High Magnetic Field Laboratory at Florida State University, Tallahassee, United States

Abstract

Anomalously high amounts of orthopyroxene are an unexpected feature of some depleted peridotite xenoliths from the cratonic lithosphere. This investigation presents new petrographic, geochemical and thermodynamic modelling data for silica-rich spinel harzburgites and one garnet–spinel harzburgite from the Kaapvaal Craton, South Africa, to constrain the pressure–temperature (P–T) conditions of orthopyroxene formation. At the time of sampling by the host kimberlite, the garnet–spinel harzburgite resided on the geotherm at 25 kbar, 765°C, wheras the compositionally similar garnet-free samples probably equilibrated at broadly comparable P–T conditions. The samples are subdivided into 'bronzite type' peridotites characterised by orthopyroxene with micrometre scale exsolutions of spinel ± clinopyroxene, and 'normal type' peridotites in which orthopyroxene does not contain visible exsolved phases. The presence of these exsolved phases indicates unmixing from a more Al-Cr-(Ca)-rich precursor orthopyroxene i.e. an original orthopyroxene that precipitated from, and was, in equilibrium with the Si-enriching agent at high temperature, before cooling and undergoing sub-solidus re-equilibration to form the exsolved orthopyroxene we observe now. Major and trace element compositions, geochemical interpretation and thermodynamic modelling of the samples show that the precursor orthopyroxene coexisted with melt at high pressure and temperature (~40–50 kbar, 1600–1700°C) within the garnet stability field. We consider these to be the conditions of orthopyroxene formation, and thus silica enrichment. These conditions, together with the refractory composition of the host peridotite (olivine forsterite contents > 92) suggest that silica enrichment is a secondary process potentially resulting from interaction with komatiitic melts. Our observations demonstrate that orthopyroxene enrichment in spinel-facies peridotites is not limited to low-pressure processes but can also occur via high-pressure melt–rock interaction, offering new insights into the thermal and chemical evolution of the sub-cratonic lithospheric mantle.

Keywords: exsolved orthopyroxene; silica enrichment; Kaapvaal craton; spinel harzburgite; thermobarometry

(Received 22 June 2025; revised 5 December 2025; accepted 14 December 2025; Accepted Manuscript published 22 December 2025)

Introduction

Archaean cratons form the cores of the Earth's modern-day continents. In some cases, the crust is underlain by a deep lithospheric mantle root, commonly termed the sub-cratonic lithospheric mantle (SCLM). The SCLM consists predominantly of peridotite, with subordinate mafic assemblages (Pearson and Nowell, 2002; King 2005; Griffin *et al.*, 2009; Brey and Shu, 2018). Peridotitic mantle xenoliths from the SCLM typically display high MgO, and low FeO, CaO, Na_2O and TiO_2 as well as low concentrations of volatile, and heat-producing elements (Herzberg, 1993; Carlson *et al.*, 2005; Griffin *et al.*, 2009). This extremely refractory composition is consistent with an origin as the residues of high degrees of partial melting of a primitive mantle and results in a lithosphere that is cool, buoyant and mechanically stable (Arndt *et al.*, 2002). These characteristics have enabled cratons to survive, at least partially, since the Archaean (Sleep, 2003).

Globally, olivine in cratonic peridotite xenoliths display a ubiquitously high Mg# (molar Mg/[Mg + Fe^{2+}]) of ~92.6 (Boyd, 1989; Bernstein *et al.*, 2007), which by comparison to partial melting experiments should be indicative of a residue with >70% modal olivine (Baker and Stolper, 1994; Walter, 1998). Nevertheless, some cratonic peridotite xenoliths have anomalously high orthopyroxene contents, beyond that expected for residues formed by partial melting of fertile peridotite mantle (Boyd, 1989). Orthopyroxene-rich peridotites have lower-than-expected MgO/SiO_2 ratios and are common in the Kaapvaal and Siberian cratons but are also present as subordinate populations in the Slave and Rae cratons (Herzberg, 1993; Gao *et al.*, 2021; Tomlinson and Kamber, 2021). The departure of silica-enriched peridotites from experimental peridotite melting trends suggests an additional silica enrichment process, during which orthopyroxene is formed at the expense

Corresponding author: Bakang Jarious Kaekane; Email: kaekaneb@tcd.ie
Guest Editor: Caterina Melai

This paper is part of a collection on Mantle Heterogeneity and Evolution

Cite this article: Kaekane B.J., Tomlinson E.L. and Hoare B.C. (2026) Quantifying the P–T conditions of silica enrichment in Archaean cratonic spinel-facies peridotites. *Mineralogical Magazine*, 1–22. https://doi.org/10.1180/mgm.2025.10188

© The Author(s), 2025. Published by Cambridge University Press on behalf of The Mineralogical Society of the United Kingdom and Ireland. This is an Open Access article, distributed under the terms of the Creative Commons Attribution licence (http://creativecommons.org/licenses/by/4.0), which permits unrestricted re-use, distribution and reproduction, provided the original article is properly cited.

of olivine. A range of models have been proposed to explain the silica enrichment of the cratonic lithosphere, many of which are related to the conditions of SCLM formation. Low-pressure models suggest initial depletion of fertile mantle to form a refractory lithospheric mantle at a mid-ocean ridge followed by serpentinisation (Canil and Lee, 2009), or alternatively interaction of crustal-derived fluid/melt with peridotite in the mantle wedge at convergent plate margins (Kesson and Ringwood, 1989; Kelemen *et al.*, 1998; Bernstein *et al.*, 2007; Simon *et al.*, 2007; Wang *et al.*, 2018). However, silica enrichment via interaction with hydrothermal or crustal derived fluids/melts (Kelemen, 1998, Canil and Lee, 2009) is challenged by the observation of silica-rich cratonic peridotites having uniformly mantle-like oxygen isotope compositions (Regier *et al.*, 2018). Furthermore, models invoking silica enrichment prior to stacking and/or compressional thickening are difficult to reconcile with the occurrence of melt-related micro-textures in silica rich peridotites (Daczko *et al.*, 2025). Silica enrichment in high-pressure SCLM formation models has been attributed to the formation of orthopyroxene-rich harzburgite cumulates during equilibrium crystallisation of melts with very high contents of silica (Herzberg, 1993). Alternatively, orthopyroxene might be added by fluid/melt–rock reaction to a depleted peridotite within the established cratonic lithosphere through 'stealth metasomatism' (O'Reilly and Griffin, 2013). For example, silica enrichment could occur when the cratonic residue interacts with upwelling mantle-derived melts (Aulbach *et al.*, 2011; Tomlinson and Kamber, 2021), or with fluids derived from basaltic melts (Branchetti *et al.*, 2021) and thus may not be linked to the original craton formation environment.

Here we present a systematic petrological, geochemical and thermodynamic investigation of a suite of silica-rich spinel-harzburgite xenoliths, one containing trace garnet, from the Bultfontein kimberlite, Kaapvaal craton. Bronzite-type orthopyroxenes contain abundant micrometre-scale exsolution lamellae of spinel ± clinopyroxene and such exsolved phases reflect the former presence of an Al-Cr-(Ca)-rich orthopyroxene precursor, formed as the result of Tschermak substitution ($Si^{4+} + M^{2+} \rightarrow 2Al^{3+}$) at high temperature and/or low pressure (Canil, 1991). As a result, precursor orthopyroxenes permit reconstruction of their P–T evolution by comparison of their reconstructed compositions with intersections of thermodynamically modelled composition isopleths and the peridotite solidus. Using this information, we can quantify the P–T conditions at which orthopyroxene formation, and thus silica addition, occurred within the Kaapvaal cratonic mantle. Thermodynamic modelling has previously been conducted on exsolved garnet-facies peridotites from the same location (Tomlinson and Holland, 2021), and we extend this work to orthopyroxene-rich spinel-facies peridotites and provide a shallow-mantle perspective on the process of silica enrichment within the Kaapvaal lithosphere.

Geological setting and background

Our samples were recovered from the ca. 84 Ma Bultfontein pipe of the Kimberley cluster (Kramers *et al.*, 1983), in the western (Kimberly) block of the Kaapvaal craton, southern Africa. The Kimberly block is delineated to the east by a 2.88 Ga Colesberg magnetic lineament, interpreted to be a surface reflection of an east–west collision and subduction beneath the Kimberly block (Schmitz *et al.*, 2004). The northern, western and southern extremities of the Kimberly block are defined by a high-grade metamorphic terrain (Limpopo belt, 2.7 Ga), the 2.1–1.8 Ga Kheis-Okwa-Magondi orogen, and the 1.3–0.9 Ga Namaqua-natal belt, respectively (de Wit *et al.*, 1992; Oriolo and Becker, 2018). A major magmatic event which occurred in the Kimberly block SCLM is the intrusion of volcanic lavas of the 2.8–2.6 Ga Ventersdorp supergroup which consists of basalts and subordinate komatiites (Schweitzer and Kröner, 1985; Gumsley *et al.*, 2020). These were emplaced after the craton underwent episodic extension between 3.1–2.7 Ga (Schoene *et al.*, 2008). The Kimberly block was also affected by a ca. 2.2 Ga failed rift and subsequently a voluminous ca. 1.11 Ga Umkondo large igneous province (LIP) expressed as mafic outcrops of the Xade and Tshane complex (Anhaeusser, 2006; de Kock *et al.*, 2014; Humbert *et al.*, 2020; Hayes *et al.*, 2024). Modification of the Kaapvaal craton probably also occurred during the eruption of the ca. 0.18 Ga Karoo-Ferrar LIP across southern Africa and Antarctica, which is voluminously comparable to the Umkondo LIP (Moulin *et al.*, 2017). Most of the kimberlite magmatism took place in the Jurassic and Cretaceous periods, including the eruption of the Bultfontein kimberlite pipe (Griffin *et al.*, 2014; Tappe *et al.*, 2018).

Samples

Thirteen silica-rich spinel harzburgites and one garnet–spinel harzburgite were selected. Samples that displayed modal metasomatism, indicated by the presence of phlogopite or amphibole, were avoided where possible during hand-specimen selection. The xenoliths typically had diameters > 10 cm. The samples were subdivided into two types: 'normal' and 'bronzite' peridotites, based on the appearance of orthopyroxene. In normal peridotites ($N = 7$), orthopyroxene has a yellowish-green appearance in hand specimen and is devoid of visible exsolutions. In bronzite peridotites ($N = 7$), orthopyroxene has a 'bronzy' appearance and contains exsolutions of spinel and/or clinopyroxene.

We use the term 'bronzite orthopyroxene' to refer to exsolved orthopyroxene and its exsolution lamellae, and the term 'precursor orthopyroxene' refers specifically to bulk orthopyroxene prior to exsolution. Additionally, the 'precursor composition' refers to the bulk composition of the orthopyroxene and its exsolutions which approximates the pre-exsolution orthopyroxene composition.

Polished sections with a ~200 μm thickness were prepared from each sample for petrographic and *in situ* geochemical analysis (Fig. 1). In addition, rock powders for whole-rock major-element analysis were prepared by removing the weathered exterior surface and then crushing and milling.

Analytical and computational methods

Three categories of geochemical data were obtained from the sample thin-sections: (1) scanning electron microscopy-energy-dispersive X-ray spectrometry (SEM-EDX) major element spot analysis of specific phases, including olivine, spinel and pyroxene in symplectite, unexsolved orthopyroxene ('normal-type' samples) or exsolved orthopyroxene (between lamellae in bronzite orthopyroxene) and individual spinel and clinopyroxene lamellae therein; (2) wide beam 'bulk' analysis of the major-element composition of the precursor orthopyroxene (orthopyroxene host plus exsolved spinel and clinopyroxene lamellae) in bronzite peridotites via laser ablation-inductively coupled plasma-mass spectrometry (LA-ICP-MS); and (3) trace-element analysis of garnet and orthopyroxene (normal peridotites) or precursor orthopyroxene (bronzite peridotites) via LA-ICP-MS. Although SEM-EDX is sometimes perceived as less quantitatively reliable than

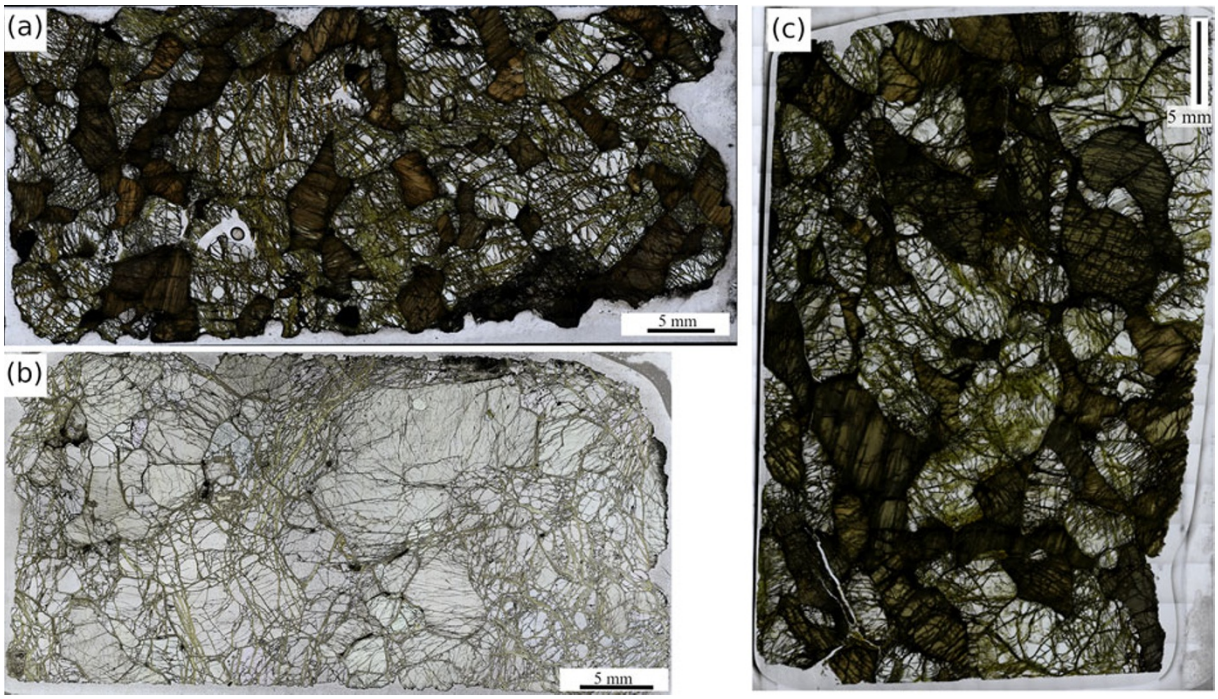

Figure 1. Plane-polarised thin-section scans which are examples of the sample types. (a) Bronzite-type spinel harzburgite which has orthopyroxene hosting spinel and clinopyroxene exsolutions (sample 13CLA066). (b) Normal-type spinel harzburgite containing orthopyroxene that is devoid of exsolved phases (sample 13CLA34). (c) Bronzite-type spinel–garnet harzburgite 17BSK039.

electron probe microanalysis-wavelength dispersive spectrometry (EPMA–WDS), recent work has emphasised that high-quality analytical results can be achieved with careful calibration and optimisation (Guyett *et al.*, 2024).

SEM-EDX

Major-element analysis was undertaken with a TESCAN TIGER SEM fitted with two 170 mm^2 Oxford Ultim Max^N detectors in the iCRAG laboratory at Trinity College Dublin (TCD), Ireland. We used a ~300 pA beam current and a 20 kV accelerating voltage to raster the electron beam over a ~5 μm area. However, for analysis of small features, e.g. exsolutions, the raster area was reduced to approach the excitation volume of the sample from the beam (~2.5 μm at 20 kV). Each analysis acquired 2 million counts. The instrument was calibrated using a series of appropriate matrix matched materials from the Astimex MINM-25-53 reference block (diopside: Si.; rutile: Ti., chromite: Al, Cr.; almandine–garnet: Fe; orthoclase: Mn.; olivine: Mg; kaersutite: Ca; tugtupite: Na; apatite: K; sphalerite: Zn; pentlandite: Ni). In addition, we analysed several reference materials from the Smithsonian National Museum of Natural History for quality control (diopside [NMNH117733], pyrope [NMNH143968], olivine [NMNH111312-44], and augite [NMNH122142]; Jarosewich *et al.*, 1980). Accuracy for elements with >1 wt.% was better than ±5% (percent bias), with the exception of Fe in pyrope which was slightly higher at <10% (Supplementary Table S1_7; Fig. S5_2). The limit of detection using this set up is 0.2 wt.% (Guyett *et al.*, 2024), however concentrations below 1 wt.% are considered semi-quantitative. The stoichiometry of all reference material and sample analyses were assessed during each analytical session as an additional check on data quality. Formula recalculation of olivine and spinel is based on 4 oxygens and pyroxene and garnet are calculated based on 6 and 12 oxygens per formula unit, respectively. Stoichiometry was better than ±0.02 atoms per formula unit (apfu) on all reference material analyses as well as all sample olivine, pyroxene and garnet analyses. We also performed multiple analyses on each grain to assess for homogeneity and analysed > 3 grains per sample to check inter-grain variations.

LA-ICP-MS

We undertook LA-ICP-MS using two different instruments: a Photon Machines Iridia 193 nm laser with a two-volume Helix cell coupled to an Agilent 7900, and a Photon Machines G2 193 nm laser with a two-volume Helix cell coupled to a Thermo iCAP Q ICP-MS, both located in the iCRAG laboratories at Trinity College Dublin, Ireland. In all cases, caution was exercised to avoid analysis on alteration and grain fractures. Data reduction was undertaken with *IOLITE4* software (Paton *et al.*, 2011).

Bulk major-element analyses

We obtained bulk major and minor element compositional data for precursor orthopyroxenes by collecting a single aerosol composed of both the exsolution lamellae and the host pyroxene. Though mixed-phase analyses may not perfectly reconstruct the original homogeneous phase, and ablating exsolved orthopyroxene carries uncertainties—for example, potential skewing of the integrated composition due to lamellae distribution within the incident beam width, our evaluation of back-scattered electron (BSE) images shows that lamellae are mostly <1 μm (occasionally up to 4 μm) and generally evenly to quasi-evenly distributed with spacing of the order of a few micrometres. For example, in sample 17BSK039, the thickest exsolutions are ~0.7 μm and are evenly distributed. Analyses were undertaken using a large laser

spot (80 µm for 13CLA36 and 100 µm for other samples) with laser repetition rates of 10 and 12 Hz, respectively, for 200 shots, equating to a vertical sampling depth of ~50 µm and so should be able to capture a representative bulk orthopyroxene composition. The low standard deviations obtained from up to 20 replicate analyses on different grains in the same sample support the robustness of the method to approximate the precursor orthopyroxene composition. Orthopyroxenes in normal peridotites were not characterised using this approach as these generally do not contain exsolutions, however we did analyse one sample (13CLA36) in order to check the accuracy of the major-element LA-ICP-MS data and successfully reproduced the results from SEM-EDX (See Results below). We analysed glass and silicate mineral reference materials: BCR-2G, BHVO-2G, GOR128-G, GOR132-G, T1G, KL2, ML3, GSD-1G (Jochum *et al.*, 2005; Jochum *et al.*, 2011) and a suite of well characterised cratonic orthopyroxene in-house reference materials (Supplementary Tables S1_7, S2_3 and S2_4). Major-element compositions were calibrated by normalising all analytes to a total of 100 wt.% using the *Trace Elements Next* data reduction scheme (DRS) in *IOLITE4*. An in-house orthopyroxene, previously characterised by EMPA (BP002), was used to calibrate elements with >1 wt.% abundance (^{29}Si, ^{57}Fe and ^{24}Mg), and GOR132-G was used to calibrate lower abundance major and minor elements. For the glass reference materials, accuracies are typically ±5% or better, but ± 8% for TiO_2. In terms of in-house standards, LA-ICP-MS data was within ±5% or better for >0.5 wt.% values obtained for the same materials via EPMA-WDS. Accuracy is within ±12% or better for concentrations > 0.5 wt.%.

Trace-element analyses

Trace elements in orthopyroxene (normal type), precursor orthopyroxene (bronzite type), garnet and symplectite were analysed with a laser repetition rate of 20 Hz using a spot size of 100–110 µm for most analyses and a 25 µm spot size for analysis of garnet. Data was reduced using the *Trace Elements DRS* in *IOLITE4* with NIST-SRM612 as the calibration standard and ^{29}Si as the internal standard, using wt.% values obtained from SEM-EDX. In the case of symplectite, the signal is composed of a mix of the constituent phases i.e. pyroxene and spinel. However, we assume that all measured trace elements reside in the pyroxene ($D^{pyroxene/spinel} \gg 1$) component and use the ^{29}Si concentration of pyroxene as the internal standard. Accuracy for glass reference standards BHVO-2G, BCR-2G, GSD-1G and GOR132-G (Jochum *et al.*, 2005) is typically better than 6% (Supplementary Table S3_2).

X-ray fluorescence analysis

Whole-rock major-element analysis was undertaken on fused beads by wavelength-dispersive X-ray fluorescence (WD-XRF) in one of two laboratories. A subset of the samples was analysed at Actlabs, Canada, where evaluation of accuracies against reference materials BIR-1, Oreas 73a, WS-E, DTS-2B and GS-N demonstrate that accuracies are better than 5% for all elements (Supplementary Table S4_1). The remaining samples 17BSK039, 13CLA21, 13CLA34, 13CLA37, 13CLA42, which were added following further sample selection, were analysed at the Earth Surface Research Laboratory at TCD using a Zetium XRF spectrometer. Reference materials JA-1a and JB-1b from the National Institute of Advanced Industrial Science and Technology (AIST) were also analysed and demonstrate that for all elements, accuracy is typically better than ±4% (Supplementary Table S4_1).

Modal abundances

Bulk rock data were combined with mineral compositions to calculate phase proportions in the xenoliths. We used SEM-EDX data to represent the compositions of the mineral phases, except for orthopyroxenes containing exsolutions where we used the bulk mineral composition determined by LA-ICP-MS. Modal phase proportions were estimated by mass balance using least-squares regression of SiO_2, Al_2O_3, Cr_2O_3, FeO_{tot}, MgO and CaO.

Phase equilibrium modelling

Pressure–temperature pseudosections were calculated with *THERMOCALC 3.50* (Powell *et al.*, 1998; updated Dec. 2020) operated via *PyPSBuilder 2.4.1* (Lexa, 2021) using the Tomlinson and Holland (2021) activity-composition models and Holland and Powell (2011) dataset tc-ds-634 under the dry system Na_2O–CaO–FeO–MgO–Al_2O_3–SiO_2–TiO_2–O–Cr_2O_3 (NCFMASTOCr). 3% of the FeO_{tot} was converted to Fe^{3+}, following Canil *et al.* (1994) who reported that average peridotite has $Fe^{3+}/\Sigma Fe = 0.03$, and Rebay *et al.* (2010) for the calculation method. A similar approach has also been applied in previous peridotitic system modelling (Jennings and Holland, 2015).

Results

Petrographic description

The samples are coarse-grained harzburgites and are primarily composed of olivine (51–65 wt.%) and orthopyroxene (34–48 wt.%) with minor spinel-pyroxene symplectites (typically < 2 wt.%). Additionally, one sample (17BSK039) contains trace garnet, clinopyroxene and spinel as discrete phases. Detailed mineral abundances are provided in Table 1. Symplectites occur in interstitial locations in the samples, usually proximal to orthopyroxene. Minor secondary minerals include serpentine, phlogopite, amphibole, secondary oxides and/or sulfides as well as micrometre-scale interstitial clinopyroxene (≪1% volume).

Olivine

Olivine occurs as 1–10 mm crystals that sporadically host tiny exsolved spinel (typically < 1 µm) (Figs 2a,b, 3a). Olivine also occurs as oval-shaped inclusions in orthopyroxene (Fig. 2c,d). Daczko *et al.* (2025) suggest that these are not inclusions but resorbed extensions of matrix olivine and that their appearance is a cross-sectioning effect, evidenced by electron backscatter diffraction (EBSD) determined crystallographic continuity of inclusions with nearby external grains. In the absence of EBSD data in this study, we retain the descriptive term 'apparent inclusions', while acknowledging that their origin may alternatively reflect the process proposed by Daczko *et al.* (2025).

Orthopyroxene

Bronzite orthopyroxenes contain abundant exsolution lamellae of spinel and clinopyroxene (Fig. 3c). These bronzitic orthopyroxene occur as blocky/elongate and lobate shaped crystals that have irregular to curvilinear grain boundaries. Grain sizes are variable within any one sample, and the size range also differs between different samples e.g. one sample displays 1–5 mm sized grains, whereas another sample contains 3–15 mm sized grains (Fig. 1a, c). Some orthopyroxene crystals terminate with low-dihedral angles. The larger crystals consistently make up most of the

Table 1. XRF bulk rock compositions and modal mineral fractions (wt.%) determined by mass-balance. With loss on ignition, totals sum to ~100 wt.%. Sample names CLA and BSK are prefixed with 13 and 17, respectively

	Bronzite-type peridotite							Normal-type peridotite						
Sample	CLA02	CLA12	CLA26	CLA29	BSK043	BSK039	CLA066	CLA03	CLA22	CLA36	CLA37	CLA42	CLA34	CLA21
SiO_2	42.40	42.55	43.20	44.83	45.04	44.69	43.58	nd	46.21	42.85	44.63	46.93	47.20	45.44
TiO_2	0.15	0.05	0.01	0.02	0.01	0.00	0.02	nd	0.01	0.01	0.00	0.02	0.01	0.01
Al_2O_3	1.32	1.35	1.28	1.67	1.67	1.70	1.05	nd	1.26	0.76	0.79	1.21	1.16	0.99
Cr_2O_3	0.35	0.34	0.33	0.37	0.39	0.35	0.33	nd	0.39	0.35	0.35	0.42	0.42	0.40
Fe_2O_3(T)	6.92	6.99	7.10	6.56	6.84	6.64	6.75	nd	6.20	6.32	6.38	6.38	6.14	6.21
MnO	0.10	0.11	0.10	0.10	0.11	0.11	0.10	nd	0.10	0.09	0.10	0.11	0.10	0.10
MgO	40.50	39.75	41.29	39.62	40.30	42.73	42.51	nd	41.21	41.93	43.50	42.37	42.86	42.64
CaO	1.50	1.10	0.91	1.21	0.94	0.76	0.38	nd	0.55	0.20	0.22	0.52	0.40	0.34
Na_2O	0.32	0.19	0.29	0.34	0.42	0.06	0.02	nd	<0.01	<0.01	0.02	0.05	0.01	0.03
NiO	0.27	0.26	0.28	0.25	0.26	0.28	0.29	nd	0.25	0.31	0.30	0.28	0.27	0.28
K_2O	0.53	0.65	0.17	0.41	0.26	0.04	0.10	nd	0.02	<0.01	nd	0.03	0.01	0.03
Total	94.37	93.34	94.96	95.39	96.24	97.35	95.12	nd	96.19	92.82	96.29	98.31	98.59	96.45
Mg#	91.3	91.0	91.2	91.5	91.3	92.0	91.8	nd	92.2	92.2	92.4	92.2	92.6	92.5
Cr#	15.1	14.5	14.7	12.9	13.5	12.0	17.4	nd	17.2	23.6	23.0	18.8	19.5	21.2
MgO/SiO_2	0.96	0.93	0.96	0.88	0.89	0.96	0.98	nd	0.89	0.98	0.97	0.90	0.91	0.94
Mineral proportions (whole rock):														
Ol	61	59	61	53	52	63	65	X	51	65	65	55	53	59
Opx	36	41	37	47	46	35	34	X	48	35	35	45	46	41
Cpx	4		2			1.4	0.1	X		0.04	0.1	0.9	0.03	0.1
Spl						0.3	0.5	X	0.5	0.4			0.5	0.4
Grt						*								
Mineral proportions (symplectite):														
Cpx						73	78, 80			78				5
Opx														72
Spl						27	22, 20			22				23

*Observed garnet in 17BSK039 was too minor to be calculated by mass balance, nd = not determined.
X = present in the sample.

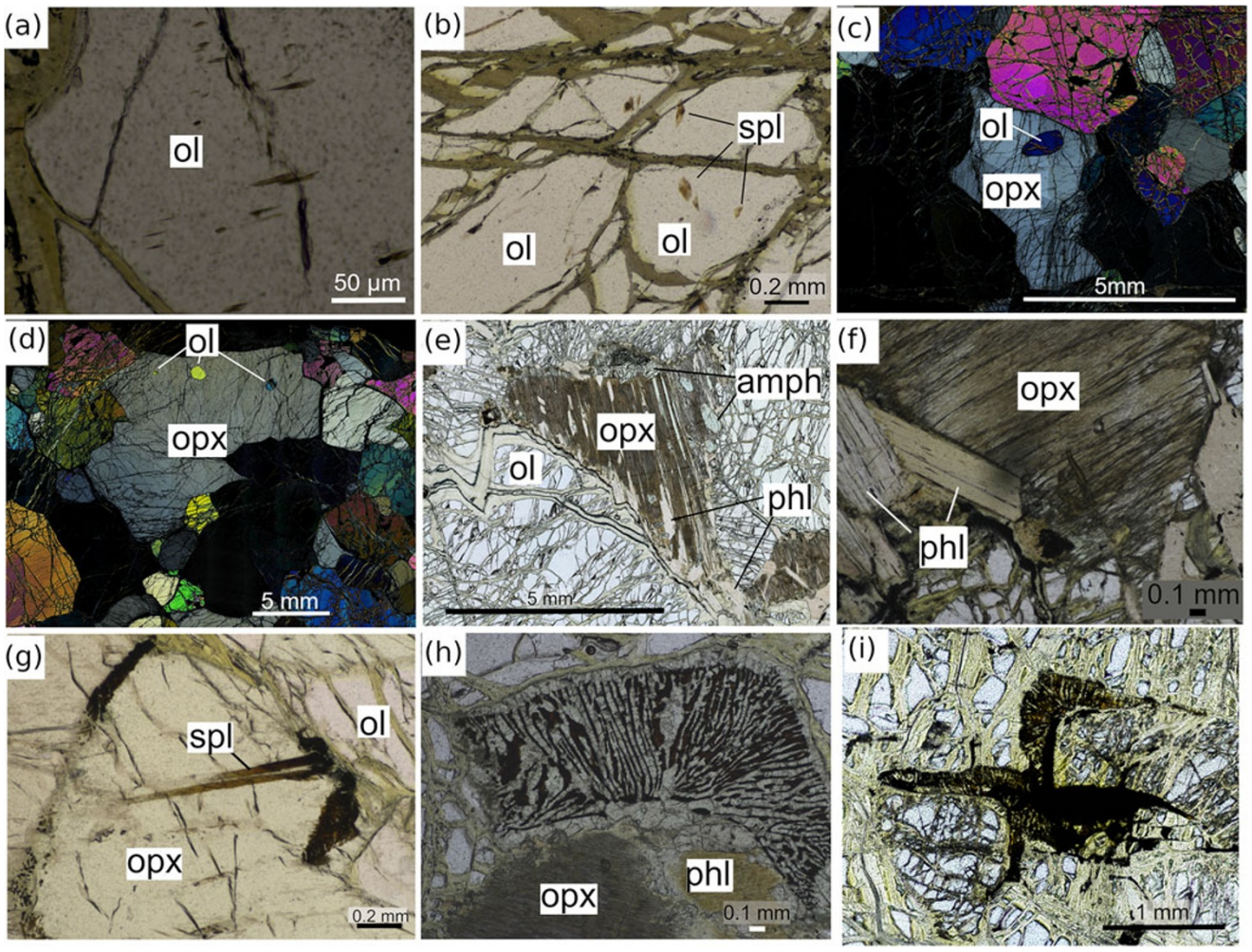

Figure 2. Selected plane-polarised (a, b, e–i) and cross-polarised (c, d) transmitted light images in the samples of this study. (a–b) Olivine containing honey-brown exsolutions of spinel in 13CLA36 and 13CLA42, respectively; (c–d) olivine inclusions in orthopyroxene under crossed polars in 13CLA03 and 13CLA34, respectively; and (e) alteration of amphibole and phlogopite on orthopyroxene in 13CLA02. Some phlogopite is seen along orthopyroxene cleavages; (f) tabular phlogopite with reaction products (opaque phase) along its cleavage in 13CLA29; (g) spinel crystallites in orthopyroxene of 13CLA37; (h) arc shaped spinel-clinopyroxene symplectite between orthopyroxene and olivine in 13CLA26; (i) irregularly shaped and branching symplectite embedded in serpentine matrix in 13CLA36.

orthopyroxene volume and are evenly distributed. The exsolved spinel and clinopyroxene are mostly < 1 µm (but occasionally as large as 4 µm) and are generally evenly distributed as separate and/or intergrown lamellae in 2D, with approximate spacing varying between 1–5 µm. However, clusters form along host orthopyroxene kinks and defects. In the least fresh samples, minor secondary amphibole/phlogopite occurs as a reaction rim around orthopyroxene and phlogopite is also occasionally observed penetrating the crystal along orthopyroxene cleavages (Fig. 2e). Sometimes phlogopite and amphibole contain opaque phases for which the identity is petrographically inconclusive, but these probably represent reaction products along the cleavages (Fig. 2f).

Normal-type orthopyroxene are characterised by euhedral-to-irregularly shaped crystals that exhibit a size ranging from 2–5 mm to 1–8 mm per sample. Exsolved phases are scarce in normal-type samples, thus when compared to bronzite orthopyroxenes, these two orthopyroxene types appear to be end-members in a spectrum of exsolved content and bronzy appearance (Fig. 3e, f). Only scarce, thin and elongate < 5 µm clinopyroxene lamellae are seen in some normal-type orthopyroxenes. Rare, thick spinel crystallites were observed to cross-cut orthopyroxene in samples 13CLA34, 13CLA36 and 13CLA37 (Fig. 2g). Unlike in the bronzite-type samples, no phlogopite–amphibole metasomatism was observed.

Garnet

A ~30 µm garnet crystal was observed within one sample only (bronzite-type sample 17BSK039). The garnet occurs as a film, located between orthopyroxene and clinopyroxene, and at the interface between two orthopyroxene crystals in two-dimensional space (Fig. 3b, c). The garnet crystal is unaltered on the interface with clinopyroxene, but minor secondary pargasite is observed along its interface with orthopyroxene.

Clinopyroxene

Granular clinopyroxene (~900 µm) in the garnet-bearing sample is observed containing exsolved spinel and thus is interpreted to be primary (Fig. 3b, c). Interstitial clinopyroxene grains (up to ~0.2 mm) are also common especially around orthopyroxene boundaries and fractures (Fig. 3h).

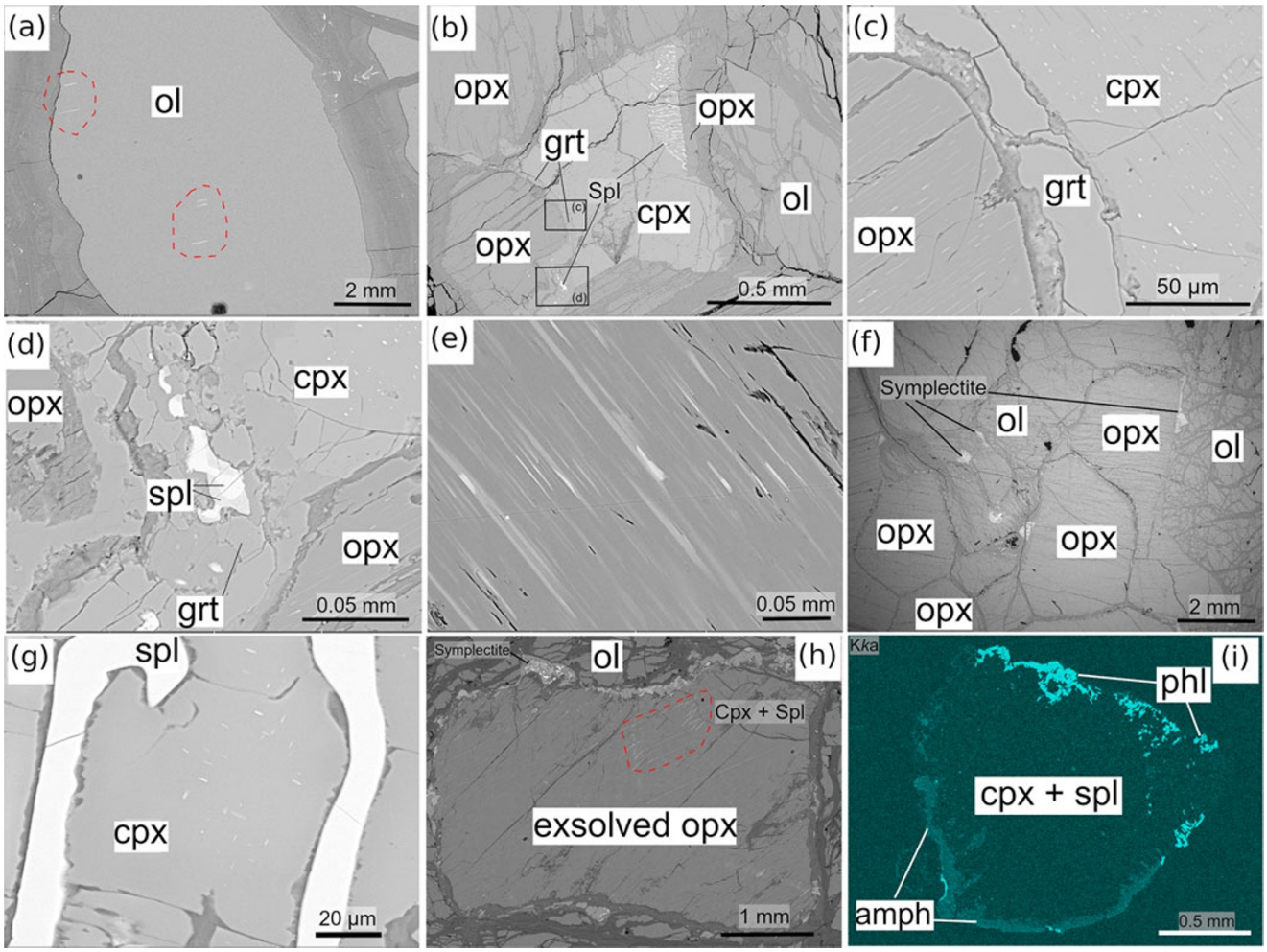

Figure 3. Selected SEM-EDX BSE images (a–h) and an element-distribution map (i) showing; (a) tiny exsolved spinel (circled red) in olivine from 13CLA36; (b) five-phase (olivine, pyroxenes, spinel, garnet) location in 17BSK039 showing a spinel-clinopyroxene symplectite between clinopyroxene and an orthopyroxene film; (c–d) close-ups of square insets illustrating a thin garnet film and an ameboid spinel characterised by Cr-rich cores. Exsolved phases are visible in granular clinopyroxene as well as orthopyroxene; (e) intergrown exsolved clinopyroxene and spinel in an orthopyroxene host from 13CLA066; (f) unexsolved orthopyroxene cluster from a normal-type sample (13CLA22). The symplectites show shape variations from sub-oval to elongate; (g) close-up of a symplectite where clinopyroxene has visible exsolutions of tiny spinel in 13CLA066; (h) exsolved orthopyroxene in bronzite sample 13CLA066, surrounded mostly by clinopyroxene crystals. Visible exsolved phases are in the red dashed area; (i) partial replacement (reaction rim) of spinel-clinopyroxene symplectite by amphibole and phlogopite in 13CLA066.

Spinel and symplectites

Small (0.1–2.5 mm) symplectites comprising the vermicular intergrowth of spinel + clinopyroxene or rarely spinel + clinopyroxene + orthopyroxene occur within all samples. They are typically interstitial between orthopyroxene and olivine but sometimes occur between olivine crystals in 2D space (Fig. 2h,3f). Most symplectites near orthopyroxene are arcuate on one side and straighter/flat on the grain boundary with orthopyroxene (Fig. 3f). Occasionally, symplectites that occur away from orthopyroxene are observed as irregular and branching features in serpentine after olivine (Fig. 2i). Clinopyroxene within symplectites may contain very tiny (< 1 µm) exsolved spinel (Fig. 3g). Phase abundances are typically represented by a 1:4 ratio of spinel to pyroxene, but when orthopyroxene is present it is the dominant pyroxene (Table 1). Amphibole/phlogopite after pyroxene is sometimes seen as patches, rims, or more rarely completely replacing pyroxene in the least fresh samples (Fig. 3i).

The garnet bearing sample 17BSK039 additionally contains discrete and ameboid spinel crystals (Fig. 3d). Discrete spinel is absent in all other samples.

Whole rock compositions

X-ray fluorescence whole-rock data are presented in Table 1. The samples show depletion in basaltic components (CaO, Al_2O_3) relative to primitive mantle. They are also characterised by high Mg#'s of 91.0–92.0 and 92.2–92.6 for bronzite and normal-type samples, respectively.

Mineral compositions

Olivine

Olivine compositions are presented in Table 2. Within a single peridotite sample, olivine has a uniform composition. The whole sample suite is characterised by a Mg# range of 92.1–93.6. Olivines within bronzite-type samples have comparatively lower Mg# values (92.1–93.0, NiO = 0.30–0.44 wt.%) than those in normal-type samples (92.8–93.6, NiO = 0.36–0.45 wt.%) (Fig. 4a; Table 2). Olivines contained as apparent inclusions in orthopyroxene have identical compositions to granular olivines within the same sample. The exception is sample 13CLA03 where the olivine

Table 2. Olivine SEM-EDX major-element compositions (wt.%) (see Supplementary data S1 for the complete dataset). Sample names CLA and BSK are prefixed with 13 and 17, respectively

Type	olivine in bronzite-type peridotites							olivine in normal-type peridotites								
Sample	CLA02	CLA12	CLA26	CLA29	BSK043	BSK039	CLA066	CLA03	CLA03*	CLA22	CLA36	CLA37	CLA37*	CLA42	CLA34	CLA21
n	11	6	10	9	6	7	36	8	9	13	16	23	3	10	7	12
SiO_2	41.25	40.99	40.62	40.84	40.63	41.21	41.24	41.45	41.57	40.64	40.78	40.78	40.62	40.89	41.11	41.52
FeO	7.20	7.75	7.34	7.36	7.37	7.06	6.86	6.75	6.51	6.67	6.66	6.91	6.81	7.07	6.33	6.95
MgO	51.38	50.47	50.62	50.22	50.73	51.01	51.04	51.66	52.02	50.87	50.82	50.70	50.69	50.82	51.55	51.82
NiO	0.35	0.36	0.37	0.40	0.30	0.44	0.43	0.41	0.45	0.39	0.42	0.38	0.36	0.44	0.38	0.44
Total	100.20	99.68	98.97	98.95	99.01	99.72	99.57	100.39	100.73	98.68	98.78	98.90	98.63	99.30	99.56	100.73
Mg#	92.7	92.1	92.5	92.4	92.5	92.8	93.0	93.2	93.4	93.1	93.2	92.9	93.0	92.8	93.6	93.0

*inclusion in olivine

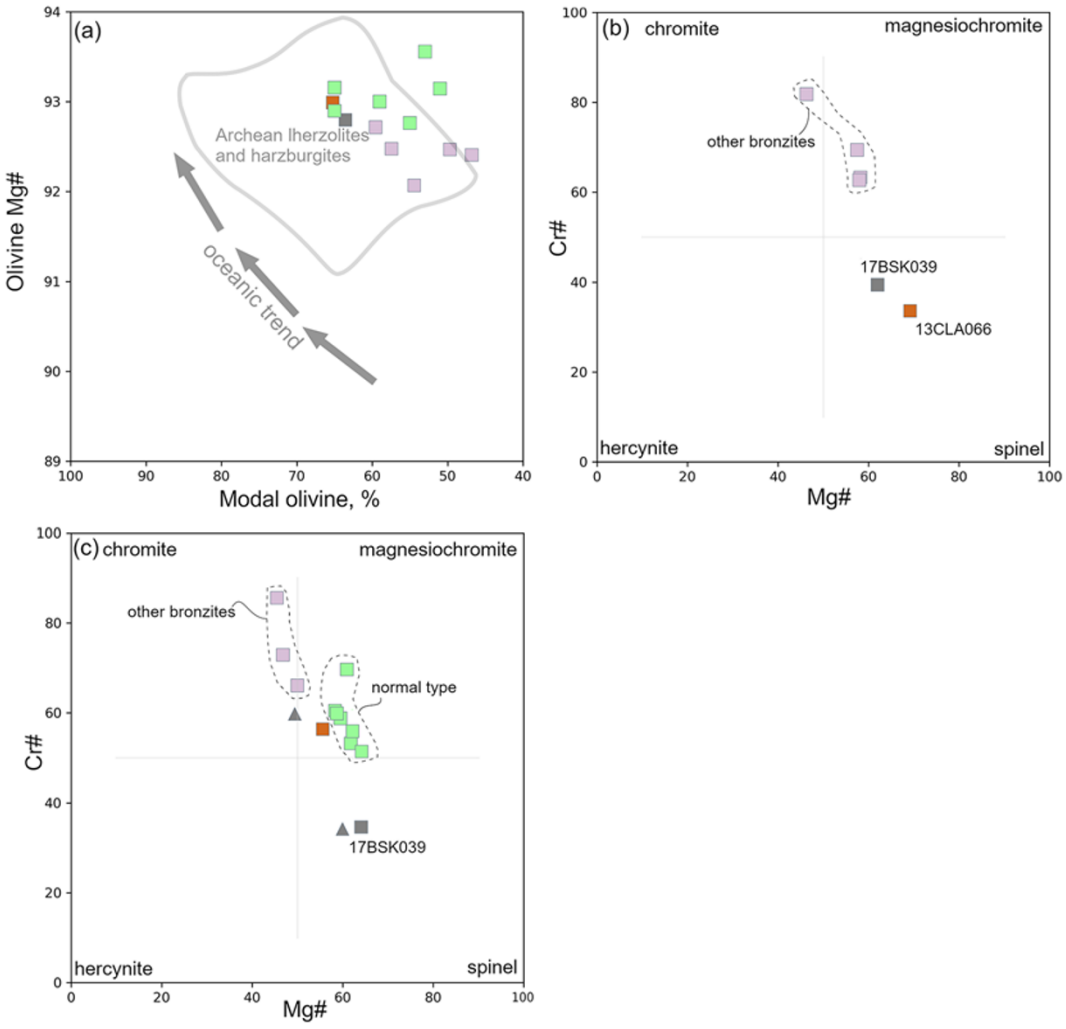

Figure 4. (a) Olivine modal proportion (wt.%) against olivine Mg#, where samples of this study plot off the oceanic partial melting trend of Boyd (1989). Archaean lherzolites and harzburgites field after Griffin *et al.* (1999); (b) compositions of spinel exsolution lamellae in orthopyroxene; (c) composition of symplectite spinels (squares). Core and rim data points (triangles) are of discrete-ameboid spinel in 17BSK039. The focus bronzite samples 13CLA066 and 17BSK039 are coloured brown and grey, respectively. Mauve, other bronzites. Green, normal-type samples.

inclusions have marginally lower FeO and higher MgO than granular olivine within the same sample (Table 2). Analysis of the sparse and tiny exsolved spinel were difficult due to their small size and attempts to extrapolate the mixed spinel–olivine compositions to SiO_2 = 0.00 wt.% was usually not successful. Only 13CLA26 olivine contained exsolved phases that were sufficiently large to be characterised as a magnesiochromite (Supplementary Figure S5_1a,b).

Orthopyroxene and its exsolved phases

Normal-type orthopyroxenes are compositionally classified as enstatites ($Wo_{1.2–1.7}En_{91.7–92.5}Fs_{6.2–6.6}$) with high Mg# (93.3–93.7) (Table 3). Al_2O_3, Cr_2O_3 and CaO values are restricted between 2.14–2.73 wt.%, 0.63–0.80 wt.% and 0.60–0.88 wt.%, respectively. LA-ICP-MS bulk composition data for sample 13CLA36 reproduces the results from SEM-EDX (Table 3). This confirms petrographic observations that exsolved phases are generally absent in normal-type samples.

Bronzite-type orthopyroxenes are enstatites ($Wo_{0.3–1.7}En_{91.2–92.8}Fs_{6.6–7.1}$) with Mg#'s ranging between 92.8–93.3. They also span a Cr# (molar $Cr^{3+}/[Cr^{3+}+Al^{3+}]$) range of 13.3–30.6. Concentrations of Al_2O_3, Cr_2O_3 and CaO (0.32–2.34, 0.21–0.59 and 0.17–0.88 wt.% respectively) extend to lower values than in normal orthopyroxenes.

Precursor orthopyroxene (i.e. orthopyroxene host and exsolution lamellae) compositions are reported in Table 3. We consider the measured precursor orthopyroxene to represent the composition of orthopyroxene in equilibrium at the solidus prior to exsolution. This approach assumes that exsolution is the only process that alters the composition of orthopyroxene, and that the orthopyroxene is not otherwise modified by exchange of slow diffusing elements or reaction with other phases in the host rock. We believe this is valid because the studied bronzite-type samples are olivine + (exsolved) orthopyroxene harzburgites, with only very minor clinopyroxene and spinel present as symplectites. As olivine and orthopyroxene do not typically exchange trivalent components, we infer that orthopyroxene acts as a closed system with respect to these components, and re-equilibration is achieved mainly by exsolution. Therefore, reconstruction of the precursor orthopyroxene by re-integrating the exsolved phases and the host is how we reverse the re-equilibration process and approximate the orthopyroxene in equilibrium at the solidus.

Table 3. Orthopyroxene major-element compositions (wt.%) (see Supplementary data S1 and S2 for the complete dataset). Sample names CLA and BSK are prefixed with 13 and 17, respectively

Type	Granular bronzite-type orthopyroxene													
Sample	CLA02	CLA02*	CLA12	CLA12*	CLA26	CLA26*	CLA29	CLA29*	BSK043	BSK043*	BSK039	BSK039*	CLA066	CLA066*
n	16	20	16	10	9	10	26	12	12	8	10	18	88	20
SiO_2	58.51	57.48	58.11	55.84	57.44	56.83	57.03	57.07	56.79	56.87	57.39	55.11	56.73	55.92
TiO_2	bdl	0.01	bdl	0.01	bdl	0.00	bdl	0.01	bdl	0.01	bdl	0.01	bdl	0.01
Al_2O_3	0.32	0.71	0.54	1.44	0.70	1.29	1.08	1.21	1.31	1.70	1.67	4.34	2.34	2.92
Cr_2O_3	0.21	0.69	0.24	0.84	0.25	0.87	0.37	0.69	0.30	0.78	0.48	0.82	0.59	0.88
FeO	4.65	4.73	4.88	5.01	4.85	5.03	4.66	4.82	4.65	4.93	4.70	4.63	4.72	4.65
MnO	0.16	0.11	0.16	0.14	bdl	0.13	0.16	0.13	0.16	0.13	bdl	0.11	0.16	0.11
MgO	36.19	34.83	35.20	34.27	35.66	34.59	34.53	34.85	35.11	34.29	35.62	32.98	35.07	34.14
CaO	0.49	0.48	0.69	1.54	0.55	0.71	0.88	0.56	0.79	0.64	0.17	1.19	0.68	0.96
Na_2O	0.32	0.28	0.36	0.57	0.18	0.23	0.36	0.22	0.29	0.33	bdl	0.07	bdl	0.04
NiO	bdl	0.05	bdl	0.06	bdl	0.07	bdl	0.07	bdl	0.06	bdl	0.09	bdl	0.08
K_2O	bdl	0.10	bdl	0.29	bdl	0.10	bdl	0.17	bdl	0.09	bdl	0.00	bdl	0.00
Total	100.07	99.48	99.92	100.04	99.21	99.86	98.90	99.81	99.00	99.83	99.89	99.35	100.05	99.71
Mg#	93.3	92.9	92.8	92.4	92.9	92.5	93.0	92.8	93.1	92.5	93.1	92.7	93.0	92.9
Cr#	30.6	42.1	23.0	28.5	19.3	28.2	18.7	27.9	13.3	23.5	16.2	11.4	14.5	16.3
En	92.2	92.0	91.4	89.6	92.0	91.0	91.2	91.6	91.5	91.2	92.8	90.4	91.6	91.1
Wo	0.9	0.8	1.3	2.9	1.0	1.4	1.7	1.1	1.5	1.2	0.3	2.3	1.3	1.7
Fs	6.6	7.0	7.1	7.3	7.0	7.4	6.9	7.1	6.8	7.4	6.9	7.1	6.9	7.0

(*Continued*)

Table 3. (*Continued.*)

Type	Granular normal-type orthopyroxene								Symplectite orthopyroxene	
Sample	CLA03	CLA22	CLA36	CLA36*	CLA37	CLA42	CLA34	CLA21	CLA03	CLA21
n	10	34	24	22	39	20	15	8	13	3
SiO_2	57.14	56.05	56.26	56.31	56.34	56.14	56.77	57.32	57.44	57.24
TiO_2	bdl	bdl	bdl	0.00	bdl	bdl	bdl	bdl	bdl	bdl
Al_2O_3	2.33	2.73	2.28	2.29	2.51	2.72	2.55	2.14	1.89	2.12
Cr_2O_3	0.76	0.75	0.71	0.75	0.79	0.80	0.76	0.63	0.79	0.69
FeO	4.31	4.28	4.35	4.35	4.37	4.41	4.23	4.43	4.64	4.63
MnO	bdl	0.15	bdl	0.10	bdl	bdl	bdl	bdl	0.17	bdl
MgO	35.39	34.44	34.62	35.42	34.66	34.33	35.19	35.33	35.54	35.20
CaO	0.62	0.80	0.60	0.64	0.62	0.88	0.73	0.65	0.43	0.54
Na_2O	bdl	bdl	bdl	0.01	bdl	bdl	bdl	bdl	bdl	bdl
NiO	bdl	bdl	bdl	0.09	bdl	bdl	bdl	bdl	bdl	bdl
K_2O	bdl	bdl	bdl	0.00	bdl	bdl	bdl	bdl	bdl	bdl
Total	100.55	99.07	98.81	99.95	99.28	99.27	100.23	100.50	100.75	100.43
Mg#	93.6	93.5	93.4	93.6	93.4	93.3	93.7	93.4	93.2	93.1
Cr#	18.0	15.6	17.3	18.0	17.4	16.5	16.7	16.5	21.9	17.9
En	92.5	91.8	92.3	92.3	92.3	91.7	92.4	92.3	92.2	92.2
Wo	1.2	1.5	1.2	1.2	1.2	1.7	1.4	1.2	0.8	1.0
Fs	6.3	6.4	6.5	6.4	6.5	6.6	6.2	6.5	6.8	6.8

*bulk LA-ICP-MS analysis of orthopyroxene precursor.
bdl = below detection limit.

In a single sample, measured precursor orthopyroxene compositions are fairly homogenous as reflected by the low standard deviations (Supplementary Table S2_1). Furthermore, based on predefined pyroxene data filtering criteria (Ziberna *et al.*, 2016., Sudholz *et al.*, 2022), the measured precursor orthopyroxenes meet the requirements of ideal stoichiometry where cation totals per six oxygens should sum to 4.000 ± 0.020. Only the measured 13CLA12 precursor orthopyroxene is non-stoichiometric because cation totals exceed 4.040. The precursor orthopyroxenes fall in the classification of enstatites ($Wo_{0.9–2.9}En_{89.6–91.9}Fs_{7.0–7.4}$), wherein the Mg# and Cr# range between 92.4–92.9 and 11.2–39.4, respectively. Precursor orthopyroxene in 17BSK039 has the highest Al_2O_3 content at 4.34 wt.% in comparison to the rest of the samples, which vary between 0.71–2.92 wt.%. Cr_2O_3 shows a more restricted range between 0.69–0.88 wt.%. CaO varies between 0.48–1.54 wt.% and positively correlates with the abundance of clinopyroxene exsolution lamellae. Comparison to the post exsolution orthopyroxenes shows that precursor orthopyroxenes have higher Al_2O_3 and Cr_2O_3 than the post exsolution orthopyroxene due to the presence of spinel. The CaO behaviour is more variable; precursor orthopyroxenes trend to higher CaO in 13CLA066 13CLA12, 13CLA26 and 17BSK039, consistent with the presence of exsolved clinopyroxene in these samples. Conversely, precursor orthopyroxenes have lower CaO than the exsolved orthopyroxene in 17BSK043, 13CLA02 and 13CLA29, consistent with the general low abundance of exsolved clinopyroxene in these samples.

Where present, the exsolved clinopyroxenes are Cr-diopsides (Table 4), albeit less chromian than the other co-existing clinopyroxene textural varieties i.e. symplectite and interstitial. The compositions of clinopyroxene exsolution lamellae occasionally fluctuate in a single orthopyroxene grain, where in some instances anomalous values may be attributed to mixed analysis e.g. CaO = 11.9 wt.% in 13CLA066. Spinel that is exsolved in bronzite-type orthopyroxenes classify as chromite, magnesiochromite or spinel (Fig. 4b). In a single orthopyroxene, spinel may display compositional variation e.g. one lamella will have a Cr# = 39.0 and Mg# = 64.0, compared to another lamella with Cr# = 31.0 and Mg# = 78.0 in sample 13CLA066. In the garnet-free bronzite 13CLA066, some exsolved phases in orthopyroxene have compositions resembling non-stoichiometric garnet.

Trace-element patterns of precursor orthopyroxene in the bronzitic samples show an overall negative trend from the most incompatible elements (Th, U, Nb, Sr, LREE) to the least incompatible elements (MREE–HREE), with negative anomalies in Ti and Zr (Fig. 5a,b). Precursor orthopyroxene in samples 13CLA02, 13CLA12 and 17BSK043 have higher incompatible element contents (ranging from 0.1–10 × primitive mantle [PM]) in contrast to those in samples 13CLA066 and 17BSK039, which have lower concentrations (0.01–1 × PM). Precursor orthopyroxenes in samples 13CLA02, 13CLA12 and 17BSK043 have La_N values of ≈ 4–8 × chondrite (CI) and approximately flat LREE trends (La/Nd_N = 1.1–1.6) with a decrease into the MREE and a flat HREE trend, giving $(Sm/Lu)_N$ = 2.9–10.6. Precursor orthopyroxene in samples 17BSK039 and 13CLA066 have La_N ≈ 0.4–0.7 × chondritic values and a negative LREE trend (La/Nd_N = 2.9–3.8), decreasing to a minima at ~Dy and followed by a positive HREE slope, giving a U-shaped pattern and $(Sm/Lu)_N$ = 0.4–0.6 (Fig. 5a,b).

Trace-element concentrations of orthopyroxenes from normal peridotites are commonly at or below the limit of detection, resulting in a spiky pattern after normalisation of constant background to the chondrite profile (Fig. 5a,b). Thus, orthopyroxenes in the normal peridotites have lower incompatible trace-element contents than those in bronzite peridotites, but concentrations reported here should be considered indicative rather than quantitative. Where quantified, they appear to show a flat MREE–HREE pattern.

Garnet

Garnet in bronzite-type sample 17BSK039 has a cratonic Cr-pyrope composition (Cr_2O_3 = 1.08 wt.%) characterised by low TiO_2 contents and an average Mg# of 80.7 (Table 5). It is a G9 garnet according to the classification of Grutter (2004). The garnet lacks the humped or sinusoidal pattern commonly seen in garnet from cratonic peridotites and more closely resembles the hypothetical 'pre-metasomatic' garnet (Stachel *et al.*, 2004) that has not previously been identified in mantle xenoliths. Garnet has low Ni and moderate to high Sc (12 ppm and 175 ppm, respectively) and low concentrations of high-field-strength elements (HFSE) with 7 ppm Y, 0.04 ppm Nb and 0.2 ppm Zr and therefore falls in the 'unmetasomatised', depleted field of Griffin *et al.* (1999). The chondrite-normalised REE pattern of the garnet shows a positive linear slope leading to strongly fractionated MREE/HREE ($(Sm/Lu)_N \leq 0.005$) and LREE/HREE ($(La/Lu)_N \approx 0.0005$) ratios. Reasonable equilibrium between garnet and orthopyroxene is indicated by Onuma plots of garnet/orthopyroxene (Fig. 6a), where the observed HREE and MREE ratios are comparable to those predicted using partition coefficients calculated at 25 kbar and 765°C (as constrained below) using the method of Sun and Liang (2013). The observed and modelled compositions diverge in the LREE due to mild secondary metasomatism, to which orthopyroxene is particularly susceptible due to its low absolute LREE content.

Spinel

Spinel from all sample types span from Al- to Cr-rich compositions (Supplementary Table S1_4). One instance of compositionally zoned spinel is seen in bronzite-type sample 17BSK039, where the cores are Cr-rich relative to the rims (Fig. 4c). Some recalculated spinel analyses depart from the ideal stoichiometry of 3 cations per 4 oxygens. In part, this is probably a result of assuming a redox state where all FeO is treated as Fe^{2+}. Deviation from ideal stoichiometry is also more pronounced in the graphically estimated compositions, where the intercept at SiO_2 = 0 wt.% is a source of error (Supplementary Fig. S5_1).

Clinopyroxene

Interstitial clinopyroxenes for all samples are classified as Cr-diopsides; they are highly magnesian (Mg# = 90.7–93.9) and tend to be relatively Na- and Ti-rich (Supplementary Table S1_3). Granular clinopyroxene containing exsolved spinel + orthopyroxene was seen in bronzite-type sample 17BSK039 (Fig. 3c). The stoichiometry of the precursor clinopyroxene is non-ideal as cation totals are ~4.046 per six oxygens (Supplementary Table S2_2). Nonetheless, it is enriched in Al, Cr, Na and poor in Si and Ca relative to the composition of post-exsolution clinopyroxene measured by SEM-EDX. This precursor notably incorporates kosmochlor (0.027 apfu) and jadeite (0.038 apfu) components, which contrasts with the respective post-exsolution Cr-diopside that contains only a jadeite component. Furthermore, the precursor clinopyroxene is enriched in LREE (La_N ~10 × CI) decreasing towards the MREE with a minimum at Dy, and then a positive HREE slope reaching chondritic Yb and Lu (Fig. 5e,f). This pattern contrasts to clinopyroxene in silica-rich garnet peridotites from the same location, which have a negative HREE trend (Simon *et al.*, 2007; Wasch *et al.*, 2009). Good equilibrium between clinopyroxene and

Table 4. Clinopyroxene major-element compositions (wt.%) (see Supplementary data S1 and S2 for the complete dataset). Sample names CLA and BSK are prefixed with 13 and 17, respectively

Type	Granular		Bronzite exsolution lamellae				Symplectite in normal and bronzite type								
Sample	BSK039	BSK039*	CLA12	CLA22	CLA22**	CLA066	CLA22	CLA34	CLA36	CLA37	CLA42	CLA066	CLA21	CLA03	BSK039
n	6	3	3	4	3	76	21	13	4	6	32	67	3	4	5
SiO_2	54.34	51.90	55.24	53.42	52.60	55.16	53.89	54.37	53.91	53.58	54.12	54.28	54.71	54.66	54.70
TiO_2	bdl	0.10	0.20	bdl	bdl	bdl	bdl	bdl	bdl	bdl	bdl	bdl	bdl	bdl	bdl
Al_2O_3	2.13	3.34	1.47	2.44	0.73	1.46	2.03	1.63	1.92	1.79	2.27	1.17	1.48	1.43	1.64
Cr_2O_3	0.94	1.27	2.07	1.14	0.50	0.42	1.24	1.13	2.01	1.33	2.04	1.09	0.86	1.11	0.99
FeO	1.55	2.08	3.04	1.14	1.71	1.46	1.20	1.30	1.64	1.44	1.84	1.49	1.43	1.41	1.58
MnO	bdl	0.06	bdl	bdl	bdl	bdl	bdl	bdl	bdl	bdl	bdl	bdl	bdl	bdl	bdl
MgO	16.70	17.83	18.44	17.41	21.45	18.03	17.14	17.86	16.69	17.44	16.87	17.20	17.81	17.89	17.04
CaO	23.18	22.20	18.35	23.32	21.46	23.72	22.99	22.81	21.67	23.48	21.48	23.88	23.73	23.89	23.35
Na_2O	0.76	0.92	1.67	0.56	0.33	0.43	0.62	0.46	0.95	0.41	1.13	0.53	0.31	0.29	0.69
NiO	bdl	0.04	bdl	bdl	bdl	bdl	bdl	bdl	bdl	bdl	bdl	bdl	bdl	bdl	bdl
Total	99.59	99.75	100.42	99.41	98.78	100.69	99.12	99.57	98.78	99.46	99.78	99.64	100.33	100.67	99.98
Mg#	95.1	93.9	91.5	96.5	95.7	95.7	96.2	96.1	94.8	95.6	94.2	95.4	95.7	95.8	95.1
Cr#	22.8	20.3	48.6	23.9	31.5	16.2	29.1	31.7	41.3	33.3	37.6	38.5	28.0	34.2	28.8
En	48.8	51.0	55.3	50.0	56.7	50.2	49.9	51.1	50.3	49.7	50.6	48.9	49.9	49.9	49.1
Wo	48.7	45.6	39.6	48.1	40.8	47.5	48.1	46.9	46.9	48.0	46.3	48.8	47.8	47.9	48.4
Fs	2.5	3.3	5.1	1.8	2.5	2.3	2.0	2.1	2.8	2.3	3.1	2.4	2.2	2.2	2.6

*bulk LA-ICP-MS analysis.
**exsolution in olivine.
bdl = below detection limit.

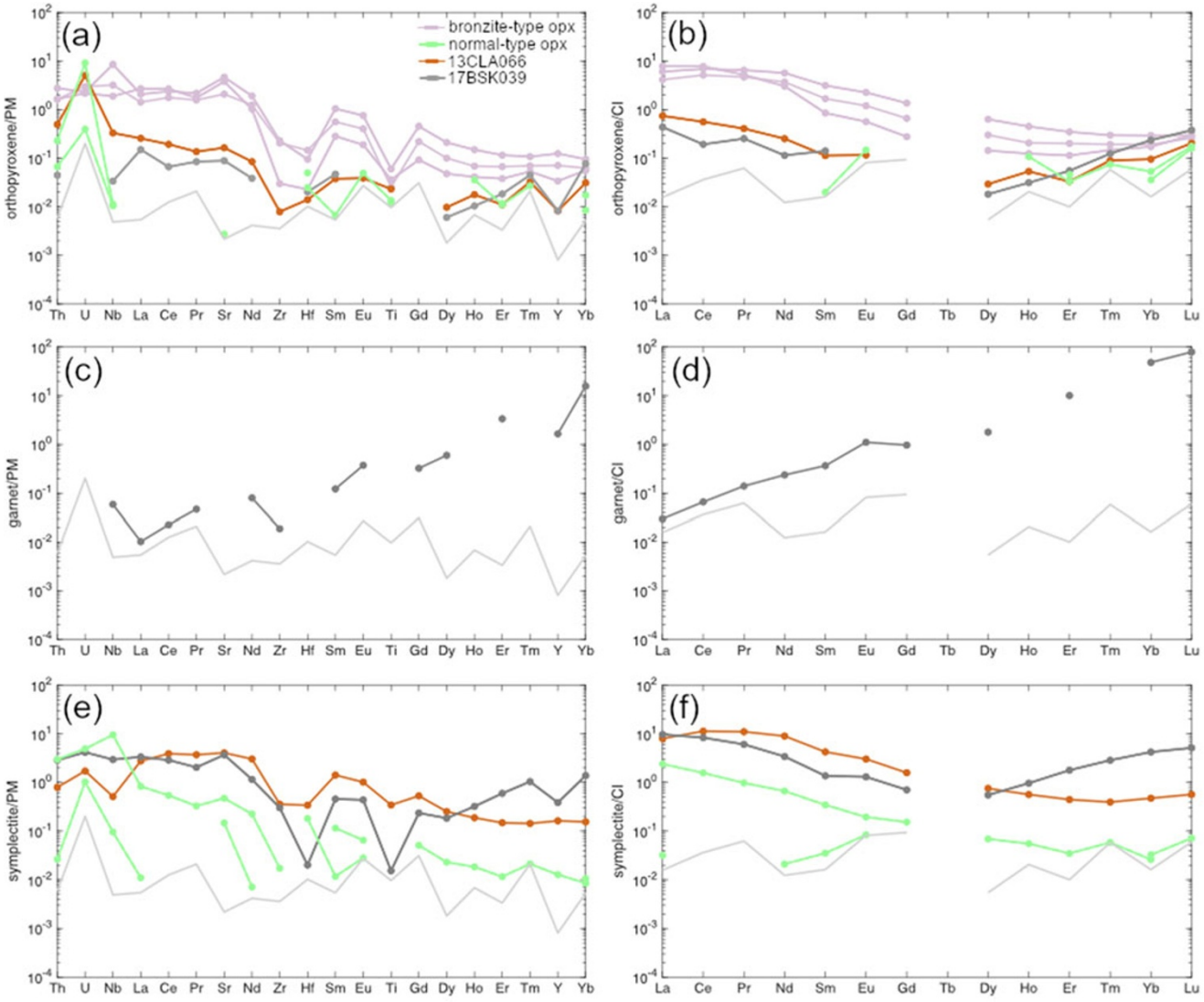

Figure 5. Averaged primitive mantle (PM; Sun and McDonough, 1989) and chondrite-normalised (CI; McDonough and Sun, 1995) trace-element plots for (a–b) orthopyroxene; (c–d) garnet; and (e–f) symplectite clinopyroxene in bronzite and normal-type samples. The limits of detection (bottom grey line) were calculated from the blank measurement average of all the sessions. Background between ablations was not suitable for the limit of detection calculation due to random spikes. The colour scheme is the same as in Fig. 4.

garnet in 17BSK039 is indicated by the agreement between the observed garnet/clinopyroxene ratio and that predicted using partition coefficients calculated at 25 kbar and 765°C (Fig. 6b) using the method of Sun and Liang (2013). This, along with the high Mg# of the clinopyroxene and the presence of exsolved phases indicates that clinopyroxene is part of the primary phase assemblage of this sample.

Symplectites

Spinel in symplectites predominantly classify as magnesiochromites or subordinately as spinel (Fig. 4c). They display a uniform composition within a specific symplectite. Some of the compositions e.g. 13CLA22 were determined by graphical analysis of spinel and its host. Occasionally, the symplectite assemblage contains enstatite which is less calcic relative to granular orthopyroxene in the same sample (Table 3). When compared to clinopyroxene exsolution lamellae in orthopyroxene, symplectite clinopyroxenes have slightly to markedly higher concentrations of Cr_2O_3 and Al_2O_3. For 17BSK039, symplectites comprise spinels that are intergrown with a Cr-diopside that is Al-poor but comparable in Mg# relative to the composition of granular clinopyroxene (Table 4).

Symplectite clinopyroxene in bronzite-type samples are weakly enriched in the most incompatible elements (Th, U, Nb, Sr, LREE), and like their coexisting orthopyroxenes, have negative anomalies at Zr and Ti. They are mildly enriched in LREE, with $La_N \approx 9$ and have gently negative LREE patterns (La/Sm_N = 2–7), reaching a minima between Tb and Tm. The HREE are either flat (13CLA066, Sm/Lu_N = 7.5) or have a positive slope (17BSK039, Sm/Lu_N = 0.3), with absolute HREE concentrations ranging between 0.4–5 × CI.

Symplectite in clinopyroxene (Fig. 5f) from normal-type sample CLA03 has a parallel pattern to 13CLA066 bronzite symplectite, but with lower absolute concentrations. Rare earth element concentrations in symplectite in CLA21 are close to or below the limit of detection.

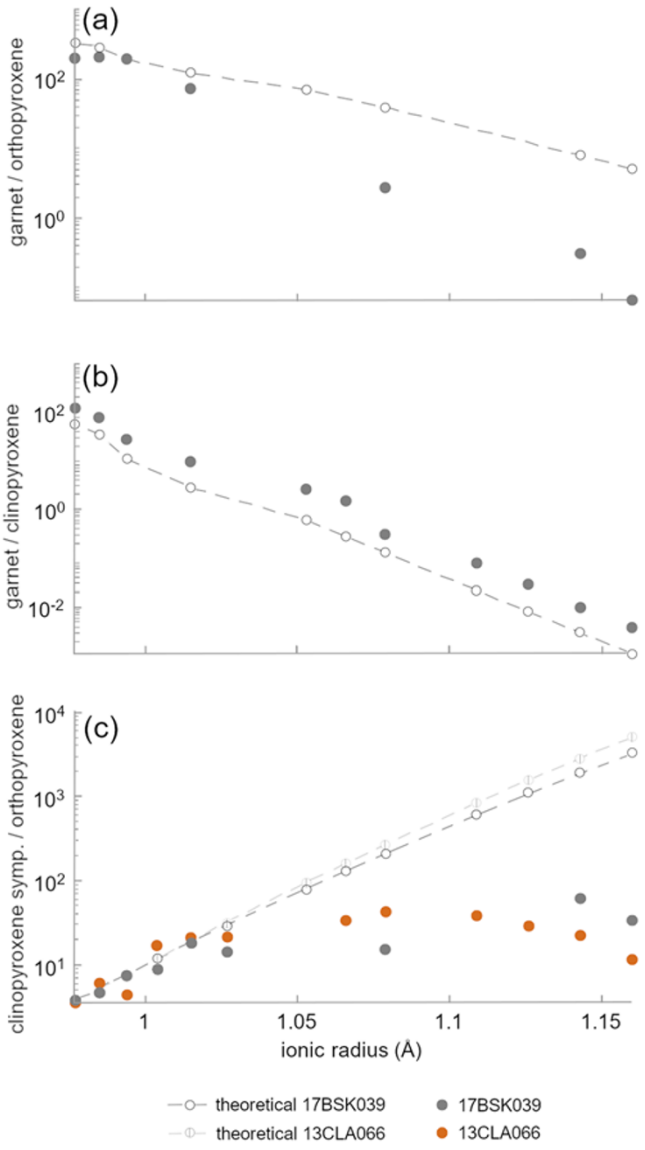

Figure 6. Onuma plots comparing observed mineral–mineral partition coefficients to theoretical values (open circles and dashed lines), calculated at 25 kbar and 765°C using the method of Sun and Liang (2013) and the observed phase bulk compositions of: (a) garnet and granular orthopyroxene in 17BSK039; (b) garnet and clinopyroxene in 17BSK039; and (c) orthopyroxene and symplectite clinopyroxene in 17BSK039 and 13CLA066. Symp stands for symplectite.

Reasonable equilibrium between symplectite clinopyroxene and orthopyroxene is demonstrated by Onuma plots of clinopyroxene/orthopyroxene (Fig. 6b), where the observed HREE and MREE ratios are comparable to those predicted using partition coefficients calculated at 25 kbar and 765°C using the method of Sun and Liang (2013), whereas patterns diverge for the LREE. In view of the equilibrium MREE–HREE compositions and the high Mg# of clinopyroxene within the symplectites, we interpret these to be part of the primary assemblage.

Equilibration P–T conditions

This study follows the Nimis and Grutter (2010) criteria to estimate the conditions of equilibration using SEM-EDX analyses and the PTEXL_2024a spreadsheet coded by T. Köhler (Stachel, 2022). Thirteen garnet-free samples presented a challenge in constraining the equilibration pressure. The Ca-in-olivine barometer (Köhler and Brey, 1990) formulated for spinel facies is deemed unsuitable here as olivine is extremely depleted in CaO (<100 ppm), which translates to analytical uncertainty being a large source of error to geobarometry. Moreover, the Ca-in-olivine barometer was calibrated in lherzolitic assemblages, where the presence of clinopyroxene (CaO buffer) is critical to the $\ln D_{Ca}^{ol/cpx}$ parameter (Köhler and Brey, 1990). The garnet-orthopyroxene barometer (Nickel and Green, 1985) coupled with the two-pyroxene thermometer (Taylor, 1998), following Nimis and Grutter (2010), shows that the garnet-bearing sample 17BSK039 records subsolidus re-equilibration at 25 kbar and 765°C.

Phase equilibrium modelling

We undertook phase equilibrium modelling of bronzite-type samples to constrain the pressure and temperature of orthopyroxene formation i.e. the P–T conditions at which silica enrichment

Table 5. Garnet SEM-EDX major-element compositions (wt.%) (see Supplementary data S1 for the complete dataset)

Sample	17BSK039
n = 7	
SiO_2	42.00
TiO_2	bdl
Al_2O_3	23.46
Cr_2O_3	1.08
FeO	8.30
MnO	0.61
MgO	19.51
CaO	5.40
Na_2O	bdl
NiO	bdl
Total	100.36
Mg#	80.7
Cr#	3.0
Py	0.7
Alm	0.2
Sps	0.0
Gr	0.1

bdl = below detection limit.

occurred. We constrain the formation conditions of the precursor orthopyroxene from intersections of the Al, Cr and Ca isopleths with the solidus. Though the use of more elements is preferable, not many suitable elements that are sensitive to changes in pressure and temperature are available. For example, the mobile Fe and Mg elements are compromised by undergoing subsolidus exchange with olivine, while Mn is not present in the thermodynamic model. For this approach, we assume that orthopyroxene formed from a melt at supersolidus conditions (supported by orthopyroxene with textures indicating former melt), and that the high Al-Cr-(Ca) precursor orthopyroxene represents the composition of orthopyroxene at the solidus – this orthopyroxene then exsolved during subsolidus cooling and re-equilibration. Therefore, LA-ICP-MS precursor orthopyroxene compositions in bronzite-type samples are ideal for investigating the P–T path taken by the sampled mantle, as the precursor orthopyroxene is assumed to reflect an earlier stage of rock evolution before sub-solidus re-equilibration. We focused on two samples: 17BSK039 (garnet–spinel harzburgite) was selected as it contains minor garnet that enabled an independent assessment of the final equilibration condition at the geotherm; 13CLA066 (spinel-harzburgite) is considered representative of the garnet-free spinel harzburgites and was selected because it has relatively well-developed exsolved phases which makes it easier to analyse. The two selected samples are fresh, having low concentrations of secondary minerals (≪1 vol.%) and low levels of incompatible element enrichment.

Equilibrium phase diagrams were calculated based on the XRF bulk compositions of each sample. The bulk XRF compositions are preferred over the recalculated bulk compositions as the latter approach is prone to uncertainty introduced by mass balancing with non-stoichiometric spinel. A potential limitation to XRF compositions is that they incorporate symplectites which are sometimes interpreted to have a secondary origin (Albee *et al.*, 1975; Smith, 1977; Field and Haggerty, 1994; Secchiari *et al.*, 2019). However, similar to a recent study (Daczko *et al.*, 2025), our textural and compositional observations indicate a primary origin of symplectites in the context of the orthopyroxene formation stage e.g. exsolutions in clinopyroxene, high Mg#'s and equilibrium with clinopyroxene symplectite/orthopyroxene in Onuma plots (Fig. 6c). Pressure–temperature pseudosections were calculated within a P–T window spanning 0–60 kbar and 600–1800°C (Fig. 7). The composition isopleths for orthopyroxene were derived from a pyroxene formula recalculated per six oxygens, where Al = ΣAl^{3+}, Cr = ΣCr^{3+} and Ca = ΣCa. As the precursor orthopyroxene represents a high-temperature phase formed at the solidus, its compositional isopleths should converge towards the solidus to indicate the conditions at which the precursor orthopyroxene was stable with melt, and by extension the conditions at which the orthopyroxene formed.

13CLA066 precursor composition isopleths are shown in Fig. 7a. Cr = 0.024 and Al = 0.12 intersect the solidus at ~47 kbar and 1700°C, within the garnet stability field in the calculated pseudosection. The large coefficient of variation (12%) in Ca results in a substantial isopleth error, which translates to the wide-spaced isopleth envelope (0.031–0.040). This envelope overlaps with the Al and Cr solidus intersections and so is permissive of orthopyroxene formation at high P–T conditions at the solidus. Additionally, the Al, Cr and Ca isopleths overlap from the solidus to ~23 kbar and ~950°C, before diverging at lower pressure. Therefore, it is possible for orthopyroxene to have formed at low to moderate pressures (between 23 and 47 kbar), however we consider formation at the solidus more likely in view of the presence of micro-textures consistent with the presence of abundant melt and the high Al_2O_3/SiO_2 content of precursor orthopyroxene (0.05), which indicates formation at high temperature (Aulbach *et al.*, 2011).

17BSK039 Cr = 0.022 and Al = 0.18 precursor composition isopleths also display a converging intersection with the solidus at ~40 kbar, 1640°C, inside the garnet stability field of the P–T pseudosection (Fig. 7b). With decreasing temperature, the Al and Cr isopleths run subparallel from the solidus at 40 kbar, crossing the garnet-out line at ~21 kbar and ~950–1050°C and continuing to lie parallel until they reach the plagioclase-in line at ~7 kbar, ~850°C. This is suggestive of formation at a broad pressure range. However, formation within the garnet stability field (i.e. >21 kbar) is supported by the steep positive HREE slopes for the bulk composition of the sample and, as with the previous sample, high formation temperatures are supported by the high Al_2O_3/SiO_2 content of precursor orthopyroxene (0.08), as well as the abundance of melt-related micro-textures (Daczko *et al.*, 2025). It is notable that neither the Ca isopleth (Ca = 0.044) nor its variation envelope intersect the modelled solidus at the pressure indicated by Al and Cr, and the Ca isopleth only crosses those of Cr and Al at ~1000°C and ~20 kbar at subsolidus conditions within the garnet field. In this regard, the bulk composition used may be inaccurate due to the extremely heterogeneous distribution of clinopyroxene in this sample, as indicated by the higher clinopyroxene content reported by Daczko *et al.*, (2025). Therefore, we weight our interpretations towards P–T conditions indicated by the Cr and Al isopleths, which are not strongly affected by the abundance of clinopyroxene.

Discussion: SCLM evolution recorded in orthopyroxene

Composition of the mantle before silica interaction

Our bronzite and normal peridotite samples have highly magnesian olivine (Mg# = 92.1–93.6), reflecting advanced degrees of melting up to 30–50% (Herzberg, 1993; Bernstein *et al.*, 2007; Pearson and Wittig, 2008). This provides a starting point for

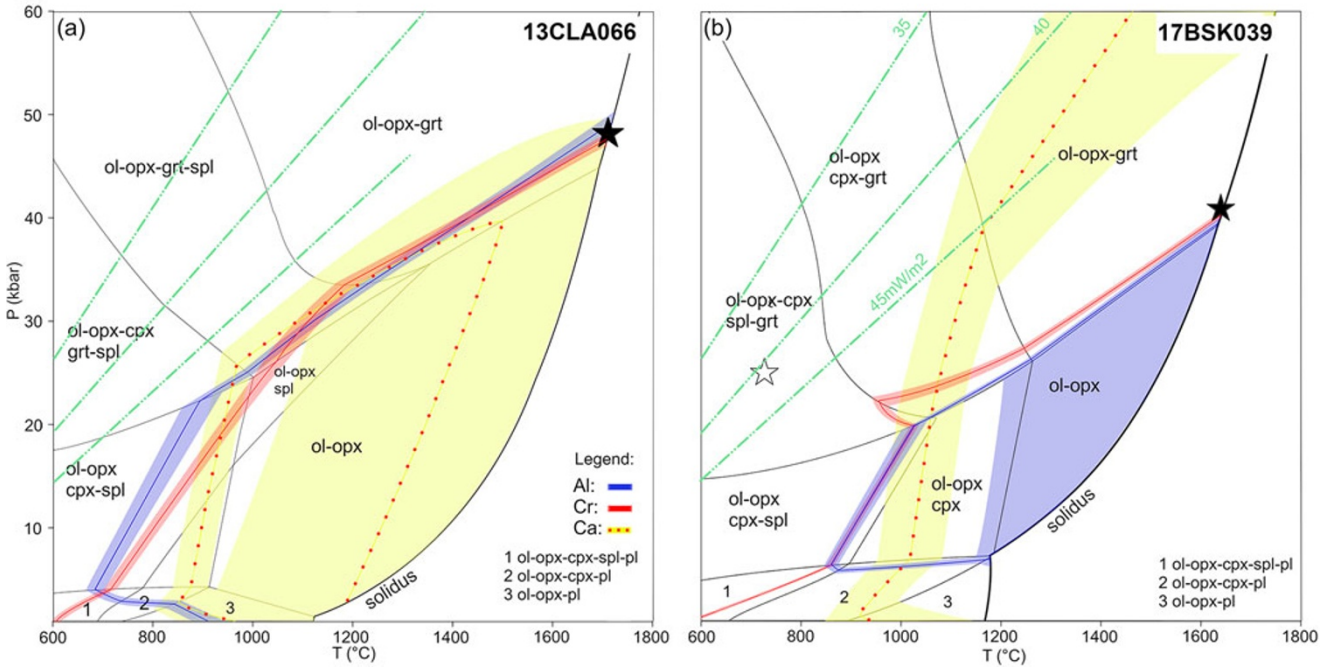

Figure 7. P–T pseudosections for selected bronzite samples, contoured with precursor composition isopleths (single line); (a) 13CLA066; and (b) 17BSK039. Each of these composition isopleths is enveloped by an uncertainty band highlighted with the same colour of the respective isopleth. Ca isopleths are stippled with red for visibility. The uncertainty bands represent the coefficient of variation calculated from LA-ICP-MS precursor analysis where Al, Ca and Cr in 13CLA066 and 17BSK039 are 3%, 3%, 12% and 2%, 1%, 18%, respectively. Dashed green lines are palaeogeotherms after Hasterok and Chapman (2011). The filled star depicts the inferred orthopyroxene formation conditions whereas the open star is the equilibration condition for 17BSK039. Grt, cpx, opx, spl and ol stand for garnet, clinopyroxene, orthopyroxene, spinel and olivine, respectively.

assessing the composition of the bulk rock composition prior to silica enrichment.

Experimental and thermodynamic modelling predict that a residue of primitive mantle melting with Mg# = 93.0 should be dominated by olivine, and have orthopyroxene contents ranging between 16–28% for initial melting at 30–60 kbar, with garnet present only at ≥ 50 kbar (Walter, 1998; Tomlinson and Holland, 2021); experimental residues produced at 10–15 kbar are orthopyroxene free at Mg# = 93 (Baker and Stolper, 1994; Falloon, 1999). Therefore, we broadly postulate a two-stage chemical evolution. Step 1 – initial high degree melting to produce a high Mg# refractory residue dominated by olivine and with only minor orthopyroxene. Step 2 – reaction with percolating melt to produce orthopyroxene at the expense of olivine. This reaction occurs at high temperature (as indicated by the formation of Al-rich orthopyroxene) and supersolidus conditions (indicated by orthopyroxene textures resembling former melt). We assume that symplectites form in step 2, perhaps from residual melt pockets (Daczko *et al.*, 2025), on the basis of their high Mg# and MREE–HREE equilibrium with garnet and orthopyroxene. Moreover, symplectites are altered or completely replaced by phlogopite (Fig. 3i), which is also seen as alteration in bronzite orthopyroxenes. Clinopyroxene in sample 17BSK039 is also considered to have formed in step 2 because of its high Mg#, MREE–HREE equilibrium with other phases and because of the presence of exsolved phases in clinopyroxene domains.

Kimberlite metasomatism

Before discussing silica enrichment, it is necessary to consider the effect of kimberlite metasomatism on the studied harzburgites. Kimberlite melt reaction results in precipitation of clinopyroxene and hydrous minerals (Grégoire *et al.*, 2002, Simon *et al.*, 2003). Also, trace phlogopite and amphibole are present in some samples which attests to later metasomatism. Metasomatism is also seen as enrichment in LREE, Th, U, Nb and Sr in all samples, but more strongly in 13CLA02, 13CLA12 and 17BSK043. The two bronzite-type samples used for phase equilibria modelling, 13CLA066 and 17BSK039, are only weakly enriched in these elements. For these samples, HREE and MREE mineral–mineral ratios match predicted partition coefficients as shown in the garnet/orthopyroxene and garnet/clinopyroxene Onuma plots (Fig. 6), although the MREE deviate from the predicted trend in the clinopyroxene/orthopyroxene Onuma plot. Therefore, we suggest that kimberlite interaction affected only the most incompatible and low concentration elements in these samples. These elements will not be used in constraining the conditions of silica enrichment.

Orthopyroxene formation conditions

We consider a scenario in which precursor orthopyroxene forms above the solidus during reactive porous flow of melt through the already depleted lithosphere (Daczko *et al.*, 2025). Subsequently, orthopyroxene experienced cooling and exsolution. The calculated P–T pseudosections reveal that final melt equilibrium with high Al-Cr-(Ca) precursor orthopyroxene occurred at ~40–50 kbar for the two samples. For 13CLA066, the pseudosection model predicts that the modal proportion of garnet in the residue at the solidus is <0.5%, with 33.8% orthopyroxene and 65.7% olivine, whereas the compositional isopleths for orthopyroxene in 17BSK039 straddle the garnet-in line (Fig. 7). In both cases, the modelled pseudosections suggest formation of orthopyroxene

within or at the periphery of the garnet stability field. An interpretation of orthopyroxene formation at sub-solidus temperatures, as suggested by the overlap of Al-Cr-(Ca) composition isopleths at low temperature (<1000°C) and below the garnet stability field is deemed implausible because of the high-Al content of the precursor orthopyroxene and the high proportion of melt indicated by the observed melt–rock micro textures.

Trace elements provide an independent tool to discriminate between the presence or absence of garnet in the bulk harzburgite at the solidus, and thus an independent check on the proposed high-pressure origin. In theory, a rock formed in the assemblage olivine–orthopyroxene–garnet will have a higher bulk-rock HREE concentration and a steep positive HREE trend. The bulk-rock HREE composition remains the same throughout subsolidus evolution in a closed system i.e. when the rock evolves from garnet-bearing to garnet-free facies, the HREE are redistributed from garnet to other phases (Sun and Liang, 2014). As our harzburgite samples are composed predominantly of olivine and orthopyroxene with only trace symplectite clinopyroxene (0.6 and 1.7 modal wt.% in 13CLA066 and 17BSK039, respectively), orthopyroxene will sequestrate HREE released by the breakdown of garnet. In contrast, a rock formed in the assemblage olivine–orthopyroxene will have a relatively low bulk-rock HREE concentration due to the absence of garnet at the time of its formation, and its orthopyroxene will remain HREE-poor throughout subsolidus evolution. Orthopyroxenes in bronzite-type samples 13CLA066 and 17BSK039 have steep positive HREE slopes ($Sm/Lu_N = 0.4–0.6$; Fig. 5) and near chondritic HREE contents, indicative of the former presence of garnet. As garnet is absent in sample 13CLA066, this suggests that garnet was consumed via subsolidus equilibration during cooling and decompression, probably by garnet reacting with olivine to form spinel and pyroxene.

Pseudosection modelling suggests that, for the samples investigated, melt–rock reaction occurred at high pressure in the garnet facies with the reacting agent originating at >120 km depth. Komatiitic melts are a plausible candidate for the reacting agent because these are MgO-rich and therefore they will not significantly reduce the Mg# of the lithosphere (Tomlinson and Kamber 2021). Additionally, they have low concentrations of incompatible trace elements which will not cause significant trace-element enrichment. Furthermore, komatiite melts are produced at high pressure and temperature (Arndt, 2003) and ascend through the Archaean lithosphere, thus they align with the modelled supersolidus conditions of orthopyroxene formation. Our observations are consistent with those of Daczko *et al.* (2025), who also investigated bronzite samples and demonstrated a mechanism for the silica enrichment reaction through stoichiometric assimilation-fractional crystallisation models: infiltrating komatiite melts initially assimilate pre-existing phases e.g. clinopyroxene/spinel/garnet and subsequently precipitate orthopyroxene/olivine upon cooling. Similarly, in experiments at 50 kbar, Melai *et al.* (2026) report formation of orthopyroxene-rich peridotite from komatiite melt that had previously fractionated olivine. If one assumes contemporaneous silica enrichment and SCLM formation (melt extraction), perhaps during the last stages, then the depth of silica enrichment can potentially infer a minimum depth of melt extraction. However, if silica enrichment occurred later, then one cannot delimit the craton formation depth based alone on the depth of excess orthopyroxene formation.

Processes during subsolidus re-equilibration

The thermodynamically constrained orthopyroxene formation pressures of ~40–50 kbar lie in the garnet stability field and are significantly deeper (at least ~15 kbar) than the conditions at which the samples equilibrated at the geotherm at the time of kimberlite eruption, constrained by the pressure of the garnet-in line along the modern geotherm. This apparent pressure change between formation and equilibration is similar to that extracted from an exsolved garnet peridotite from the same location (Tomlinson *et al.*, 2018).

After formation, orthopyroxene in the SCLM underwent mineralogical evolution (subsolidus equilibration) towards the final equilibration P–T conditions at the geotherm. This change involves cooling by ~800°C and a pressure change of 15–20 kbar. Generally, the evolution from precursor to post-exsolution composition is subtly different for the garnet-free and garnet-bearing samples. In the garnet-bearing bronzite sample (17BSK039), there is a proportional reduction of Al_2O_3 and Cr_2O_3 during the evolution from precursor to re-equilibrated orthopyroxene, which results in exsolution of aluminous spinel + clinopyroxene (Fig. 8a). In some garnet-free bronzite samples, orthopyroxene during cooling sees a decrease in Cr_2O_3 with a relatively minor change in Al_2O_3 (Fig. 8a). This is because such samples mainly host exsolved chromite that draw substantial Cr_2O_3 from the host (e.g. 13CLA02, 17BSK043, Supplementary Table S5_4). By contrast, in other garnet-free bronzite samples (e.g. 13CLA12, 13CLA066), orthopyroxene undergoes a decrease in both Cr_2O_3 and CaO and contains exsolution lamellae of both spinel and clinopyroxene. Our interpretation of these contrasting chemical trends and exsolution configurations, i.e. spinel only versus spinel + clinopyroxene, is that orthopyroxenes containing only spinel exsolution lamellae did not reach the required clinopyroxene saturation to trigger its exsolution. This saturation threshold would be reached through a process of cooling (CaO solubility in orthopyroxene; Lindsey, 1983) or cooling coupled with 'solely' spinel exsolution (enrichment of CaO in residual post-exsolution orthopyroxene). In samples where orthopyroxenes contain both spinel and clinopyroxene lamellae, we propose they reached clinopyroxene saturation either from experiencing a relatively larger cooling interval or by extensive spinel exsolution. The latter would imply that spinel was the first phase to exsolve. Selective exsolution of spinel drives the residual post-exsolution orthopyroxene to slightly higher CaO concentrations (Fig. 8b). Therefore, orthopyroxene can cool and exsolve while there is an increase in its residual CaO concentration. This is not consistent with the general notion that cooling of pyroxene decreases its CaO concentration, casting implications on geothermometry with Ca-in-orthopyroxene formulations.

Orthopyroxenes in normal-type samples tend to be more fertile relative to extensively exsolved bronzite orthopyroxenes (Fig. 8 a,b) and are more comparable to the bronzitic precursor orthopyroxene compositions. As they are mostly devoid of exsolved phases, normal-type orthopyroxenes may have been subjected to rapid cooling. Such a scenario is not conducive to exsolution occurrence and therefore results in the freezing of components which would have exsolved during slower cooling. Conversely, bronzite-type 17BSK039 shows the largest compositional variation between precursor and post-exsolution composition in terms of Al_2O_3, Cr_2O_3 and CaO. This correlates with its large cooling interval from ≈1600°C, 40 kbar down to 765°C, 25 kbar.

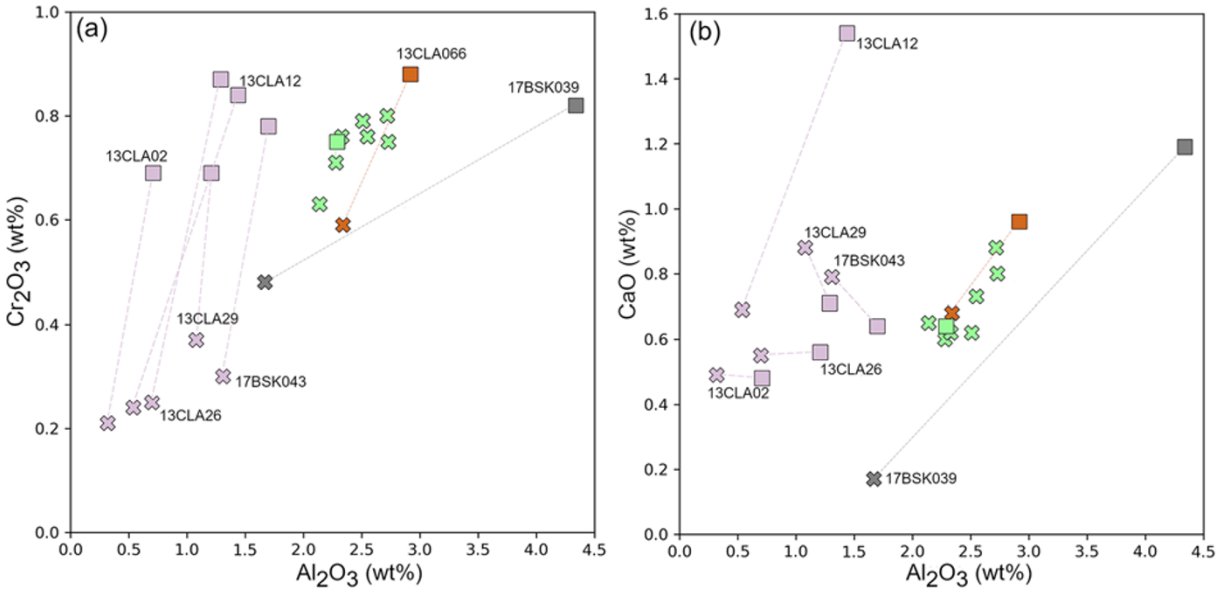

Figure 8. Orthopyroxene precursor and post-exsolution composition bivariate plots showing the relationship between Al_2O_3 and (a) Cr_2O_3; or (b) CaO. Precursor, square. Post-exsolution, cross. The samples are labelled, and the colour scheme is the same as in Fig. 4.

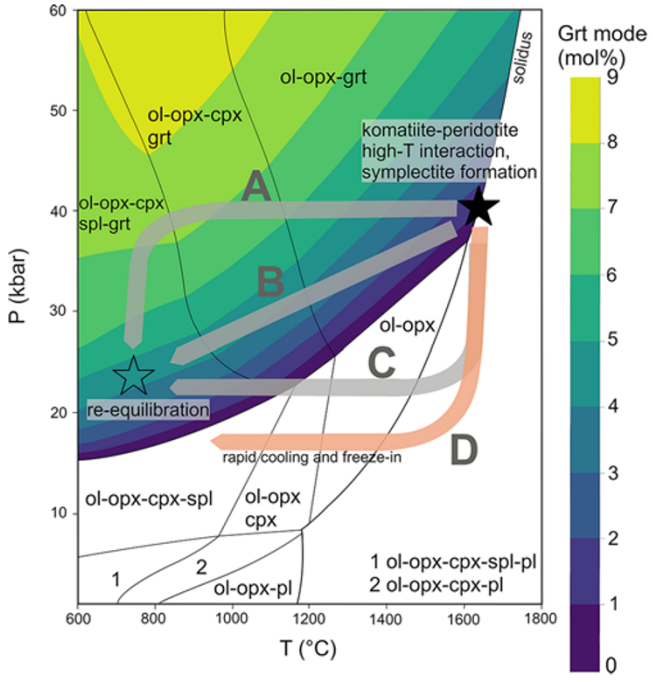

Figure 9. Possible P–T paths from the high-temperature magmatic stage (filled star) towards re-equilibration at the geotherm (open star). The P–T pseudosection topology is that of 17BSK039 and the garnet-stability field has thematic contours of garnet modal abundance.

We can use the observed exsolutions and the modelled pseudosection to speculate on the P–T path taken from orthopyroxene formation at ~40–50 kbar within the garnet facies, to final P–T conditions on the geotherm at 15–25 kbar within the spinel facies. This can be seen in Fig. 9, where we use the pseudosection of sample 17BSK039 to represent the stability of phases in the silica-rich bronzitic peridotites:

Path A depicts initially isobaric cooling followed by isothermal depressurisation and so may represent cooling from a heating event followed, possibly sometime later, by lithospheric thinning perhaps during the failed rift event at 2.2 Ga (Humbert *et al.*, 2020). As the samples studied here are mostly garnet-free, it is unlikely that the mantle evolved through path A as this is expected to generate more garnet. Although the decompression through path A would have the capability to break down garnet into symplectites, our calculations indicate that 4/5 symplectite bulk compositions are not consistent with them being retrograde products of garnet (Supplementary Table S6_1). Moreover, isothermal depressurisation is predicted to enrich orthopyroxene in Cr at any sub-solidus temperature (Supplementary Table S5_3), an observation which is inconsistent with measured high-Cr precursor orthopyroxenes evolving to low-Cr post-exsolution orthopyroxenes (Fig. 8a).

Path B considers concurrent cooling and depressurisation as may be expected if lithospheric extension and thinning was related to komatiite emplacement in the case where lithospheric heating was significant and/or protracted. This cooling trajectory can preserve garnet that was present at the solidus, as its path is sub-parallel to garnet mode isopleths and terminates in the garnet-stability field, corresponding to the assemblage in 17BSK039. Moreover, the evolution through path B is compatible with transformation of spinel from Cr-rich to Al-spinel, as seen in zoned spinel in 17BSK039 (Fig. 3d). However, because we do not observe garnet exsolutions in the samples, it is unlikely that this evolution path was followed by our mantle samples.

Paths C and D show initial depressurisation followed by cooling and may also be consistent with concurrent lithospheric thinning and komatiite emplacement in the case where the heating event was more transient and/or localised. An evolution through Path C is compatible with all samples. An initial decompression causes an exit from the garnet stability field resulting in a spinel-facies peridotite assemblage. Subsequently, slow cooling results in formation of exsolved phases, e.g. in 17BSK039, clinopyroxene is predicted to exsolve before spinel, though the 13CLA066 pseudosection model predicts that spinel would exsolve before

clinopyroxene (Fig. 7). 17BSK039 cools to 765°C, allowing the sample to re-enter the garnet facies. Garnet observed between pyroxenes in 17BSK039 also forms a partial envelope around discrete spinel (Fig. 3d) and this can be interpreted as the result of spinel breaking down to form garnet along the cooling segment of path C i.e. from the spinel facies into the spinel–garnet facies. Moreover, because 17BSK039 garnet has an un-metasomatised rare earth element pattern (Fig. 5d), the garnet either formed at a depth that is too shallow to be affected by metasomatism, or the peridotite was still in the spinel facies during the typical metasomatism affecting harzburgites where the resultant garnet has humped or sinusoidal REE patterns (Stachel *et al.*, 2004), and so spinel breakdown to form garnet occurred after this metasomatic event. In contrast, we interpret that the garnet-free samples e.g. 13CLA066, had their cooling interval terminated in the garnet-free facies at relatively higher temperatures through path C or D. Moreover, the cooling paths probably vary in range, where samples with orthopyroxene that contain both exsolved clinopyroxene and spinel have cooled to significantly lower temperatures than those with only exsolved spinel. Normal-type samples may have evolved along path C without sufficient cooling to permit exsolution, or they may have followed path D, experiencing rapid cooling at shallow depths. A plausible geological event to achieve this is transit by melts to shallow depths where low ambient temperatures result in kinetic impediment of exsolution components.

Conclusions

This study investigates the origin of silica enrichment and evolution of depleted garnet–spinel and spinel harzburgite xenoliths from the Kaapvaal craton, through integrated petrographic, geochemical and thermodynamic modelling. We conclude that orthopyroxene enrichment occurred at high pressure and temperature conditions between ~40–50 kbar and ~1600–1700°C, demonstrating super-solidus conditions for melt–rock reaction in the garnet stability field. Prior residence in the garnet stability field is supported by steep orthopyroxene HREE trends. It is inferred that orthopyroxene was added to a previously depleted peridotite via melt–rock interaction. Komatiitic melts are identified as the most plausible agents to induce the silica enrichment, as supported by the high formation temperatures for orthopyroxene and the high Mg# of the peridotites. Exsolution textures, along with the breakdown of spinel to garnet in 17BSK039 indicate subsolidus evolution along a decompression-cooling P–T path following melt–rock interaction. Moreover, the relatively low P–T conditions recorded at the time of kimberlite entrainment require that the peridotites underwent decompression. Our results therefore underscore the capability of high-pressure (> 30 kbar) processes in generating excess orthopyroxene in cratonic peridotites. Precursor orthopyroxene compositions thus provide valuable constraints at spinel-facies conditions on the thermal and chemical evolution of the sub-cratonic lithospheric mantle.

Supplementary material. The supplementary material for this article can be found at https://doi.org/10.1180/mgm.2025.10188.

Acknowledgements. The authors extend their gratitude to Peter Kelemen and two anonymous reviewers for their constructive comments, as well as to Helen Kerbey and Caterina Melai for editorial handling. We thank Dr Paul Guyett for assistance with SEM-EDX analysis.

Funding. This research was funded by the European Union (ERC-CoG-2020 LITHO3, 101044276 to ELT). Views and opinions expressed are however those of the authors only and do not necessarily reflect those of the European Union or the European Research Council. Neither the European Union nor the granting authority can be held responsible for them. The iCRAG SEM-EDX and LA-ICP-MS laboratories at Trinity College Dublin received funding from Science Foundation Ireland (SFI) awards 13/RC/2092 and 13/RC/2092-P2. Bulk rock analyses were supported by the Geological Survey Ireland-funded Earth Surface Research Laboratory in Trinity College Dublin.

Competing interests. The authors declare none.

Data availability statement. All geochemical data are available in the article and provided in the supplementary material. Geochemical data have also been submitted to the EarthChem data repository (https://earthref.org/ERDA/2774/) .

References

Albee A.L., Chayes F. and Peck L.C. (1975) Symplectites and the process of devitrification in glassy volcanic rocks. *American Mineralogist*, **60**, 256–266.

Anhaeusser C.R. (2006) Ultramafic and mafic intrusions of the Kaapvaal Craton. Pp. 95–134 in: *The Geology of South Africa* (Johnson MR, Anhaeusser CR, Thomas RJ, editors). Council for Geoscience, South Africa.

Arndt N.T. (2003) Komatiites, kimberlites, and boninites. *Journal of Geophysical Research*, **108**, 1–11.

Arndt N.T., Lewin É. and Albarède F. (2002) Strange partners: formation and survival of continental crust and lithospheric mantle. *Geological Society of London Special Publications*, **199**, 91–103.

Aulbach S., Stachel T., Heaman L.M., Creaser R.A. and Shirey S.B. (2011) Formation of cratonic subcontinental lithospheric mantle and complementary komatiite from hybrid plume sources. *Contributions to Mineralogy and Petrology*, **161**, 947–960.

Baker M.B. and Stolper E.M. (1994) Determining the composition of high pressure mantle melts using diamond aggregates. *Geochimica et Cosmochimica Acta*, **58**, 2811–2827.

Bernstein S., Kelemen P.B. and Hanghøj K. (2007) Consistent olivine Mg# in cratonic mantle reflects Archean mantle melting to the exhaustion of orthopyroxene. *Geology*, **35**, 459–462.

Boyd F.R. (1989) Compositional distinction between oceanic and cratonic lithosphere. *Earth and Planetary Science Letters*, **96**, 15–26.

Branchetti M., Zepper J.C.O., Peters S.T.J., Koornneef J.M. and Davies G.R. (2021) Multi-stage garnet formation and destruction in Kimberley harzburgitic xenoliths, South Africa. *Lithos*, **390–391**, 1–20.

Brey G.P. and Shu Q. (2018) The birth, growth and ageing of the Kaapvaal subcratonic mantle. *Mineralogy and Petrology*, **112**, 23–41.

Canil D. (1991) Experimental evidence for the exsolution of cratonic peridotite from high-temperature harzburgite. *Earth and Planetary Science Letters*, **106**, 64–72.

Canil D. (1992) Orthopyroxene stability along the peridotite solidus and the origin of cratonic lithosphere beneath southern Africa. *Earth and Planetary Science Letters*, **111**, 83–95.

Canil D. and Lee C-T.A. (2009) Were deep cratonic mantle roots hydrated in Archean oceans? *Geology*, **37**, 667–670.

Canil D., O'Neill H.St.C., Pearson D.G., Rudnick R.L., McDonough W.F. and Carswell D.A. (1994) Ferric iron in peridotites and mantle oxidation states. *Earth and Planetary Science Letters*, **123**, 205–220.

Carlson R.W., Pearson D.G. and James D.E. (2005) Physical, chemical, and chronological characteristics of continental mantle. *Reviews of Geophysics*, **43**, 1–24.

Daczko N.R., Kamber B.S., Gardner R.L., Piazolo S. and Cathey H.E. (2025) Signatures of komatiite reactive melt flow through the Archaean Kaapvaal cratonic mantle. *Contributions to Mineralogy and Petrology*, **180**, 1–25.

De Kock M.O. *et al.* (2014) Dykes of the 1.11Ga Umkondo LIP, Southern Africa: Clues to a complex plumbing system. *Precambrian Research*, **249**, 129–143.

de Wit M.J., Roering C., Hart R.J., Armstrong R.A., de Ronde C.E.J., Green R.W.E., Tredoux M., Peberdy E. and Hart R.A. (1992) Formation of an Archaean continent. *Nature*, **357**, 553–562.

Falloon T.J., Green D.H. and Hess P.C. (1999) Experimental constraints on the origins of alkali basalts and the composition of mantle sources. *Earth and Planetary Science Letters*, **168**, 173–188.

Field S.W. and Haggerty S.E. (1994) Symplectites in upper mantle peridotites: Development and implications for the growth of subsolidus garnet, pyroxene and spinel. *Contributions to Mineralogy and Petrology*, **118**, 138–156.

Gao M., Wang C., Xu H. and Zhang J. (2021) Experiment constraints on orthopyroxene enrichment in the Kaapvaal craton lithospheric mantle. *Chemical Geology*, **562**, 1–13.

Grégoire M., Bell D.R. and Le Roex, A. (2002) Trace element geochemistry of phlogopite-rich mafic mantle xenoliths: Their classification and their relationship to phlogopite-bearing peridotites and kimberlites revisited. *Contributions to Mineralogy and Petrology*, **142**, 603–625.

Griffin W.L., O'Reilly S.Y. and Ryan C.G. (1999) The composition and origin of sub-continental lithospheric mantle. Mantle Petrology: Field Observations and High Pressure Experimentation: A Tribute to Francis R. (Joe) Boyd. *Geochemical Society, Special Publication*, **6**, 13–45.

Griffin W.L., O'Reilly S.Y., Afonso JC. and Begg G.C. (2009) The Composition and Evolution of Lithospheric Mantle: a Re-evaluation and its Tectonic Implications. *Journal of Petrology*, **50**, 1185–1204.

Griffin W.L., Batumike J.M., Greau, Y., Pearson N.J., Shee S.R. and O'Reilly S.Y. (2014) Emplacement ages and sources of kimberlites and related rocks in southern Africa: U–Pb ages and Sr–Nd isotopes of groundmass perovskite. *Contributions to Mineralogy and Petrology*, **168**, 1–13.

Gumsley A., Stamsnijder J., Larsson E., Söderlund U., Naeraa T., De Kock M., Sałacińska A., Gawęda A., Humbert F. and Ernst R. (2020) Neoarchean large igneous provinces on the Kaapvaal Craton in southern Africa re-define the formation of the Ventersdorp Supergroup and its temporal equivalents. *Geological Society of America Bulletin*, **132**, 1829–1844.

Guyett P. C., Chew D., Azevedo V., Blennerhassett L. C., Rosca C. and Tomlinson E. (2024) Optimizing SEM-EDX for fast, high-quality and non-destructive elemental analysis of glass, *Journal of Analytical Atomic Spectrometry*, **39**, 2565–2579.

Hasterok D. and Chapman D. S. (2011) Heat production and geotherms for the continental lithosphere. *Earth and Planetary Science Letters*, **307**, 59–70.

Hayes B. Ashwal L.D., Khumalo K.B. and Iaccheri L.M. (2024) Major, trace element and Sr-Nd isotope evidence for a sublithospheric mantle source for the Umkondo large igneous province. *Geoscience Frontiers*, **15**, 1–23.

Herzberg C.T. (1993) Lithosphere peridotites of the Kaapvaal craton. *Earth and Planetary Science Letters*, **120**, 13–29.

Holland T.J.B. and Powell R. (2011) An improved and extended internally consistent thermodynamic dataset for phases of petrological interest, involving a new equation of state for solids: THERMODYNAMIC DATASET FOR PHASES OF PETROLOGICAL INTEREST. *Journal of Metamorphic Geology*, **29**, 333–383.

Humbert F., Agangi A., Massuyeau M., Elburg M.A., Belyanin G., Smith A.JB., Iaccheri L.M., Coetzee L and Wabo H. (2020) Rifting of the Kaapvaal Craton during the early Paleoproterozoic: Evidence from magmatism in the western Transvaal subbasin (South Africa). *Precambrian Research*, **342**, 1–22.

Jarosewich E., Nelen J.A. and Norberg J.A. (1980) Reference Samples for Electron Microprobe Analysis. *Geostandards Newsletter*, **4**, 43–47.

Jennings, E. and Holland, T.J.B. (2015) A simple thermodynamic model for melting of peridotite in the system NCFMASOCr. *Journal of Petrology*, **56**, 869–892.

Jochum K.P., Willbold M., Raczek I., Stoll B. and Herwig K. (2005) Chemical Characterisation of the USGS Reference Glasses GSA-1G, GSC-1G, GSD-1G, GSE-1G, BCR-2G, BHVO-2G and BIR-1G Using EPMA, ID-TIMS, ID-ICP-MS and LA-ICP-MS. *Geostandards and Geoanalytical Research*, **29**, 285–302.

Jochum K.P., Weis U., Stoll B., Kuzmin D., Yang Q., Raczek I, Jacob D.E., Stracke A., Birbaum K., Frick DA., Günther D. and Enzweiler J. (2011) Determination of reference values for NIST SRM 610–617 glasses following ISO guidelines. *Geostandards and Geoanalytical Research*, **35**, 397–429.

Kelemen P.B., Hart S. R. and Bernstein S. (1998) Silica enrichment in the continental upper mantle via melt/rock reaction. *Earth and Planetary Science Letters*, **164**, 387–406.

Kesson S.E. and Ringwood A.E. (1989) Slab-mantle interactions. *Chemical Geology*, **78**, 97–118.

King S. (2005) Archean cratons and mantle dynamics. *Earth and Planetary Science Letters*, **234**, 1–14.

Köhler T.P. and Brey G.P. (1990) Calcium exchange between olivine and clinopyroxene calibrated as a geothermobarometer for natural peridotites from 2 to 60 kb with applications. *Geochimica et Cosmochimica Acta*, **54**, 2375–2388.

Kramers J.D., Roddick J.C.M. and Dawson J.B. (1983) Trace element and isotope studies on veined, metasomatic and "MARID" xenoliths from Bultfontein, South Africa. *Earth and Planetary Science Letters*, **65**, 90–106.

Lexa O. (2021) *PyPSbuilder: Not that simplistic THERMOCALC front-end for constructing and visualizations of P-T, T-X and P-X pseudosections*. Retrieved from https://github.com/ondrolexa/pypsbuilder.

Lindsey D.H. (1983) Pyroxene thermometry. *American Mineralogist*, **68**, 477–493.

McDonough W.F. and Sun S. (1995) The composition of the Earth. *Chemical Geology*, **120**, 223–253.

Melai C., Withers A.C., Guyett P. and Tomlinson E.L. (2026) Experimental investigation of the role of komatiite-peridotite interaction in generating silica enrichment in the cratonic lithosphere. *Mineralogical Magazine*, **89**, doi: https://doi.org/10.1180/mgm.2026.10206.

MoulinM., FluteauF., CourtillotV., MarshJ., DelpechG., QuidelleurX. and GérardM. (2017) Eruptive history of the Karoo lava flows and their impact on Early Jurassic environmental change. *Journal of Geophysical Research: Solid Earth*, **122**, 738–772.

Nickel K.G. and Green D.H. (1985) Empirical geothermobarometry for garnet peridotites and implications for the nature of the lithosphere, kimberlites and diamonds. *Earth and Planetary Science Letters*, **73**, 158–170.

Nimis P. and Grütter H. (2010) Internally consistent geothermometers for garnet peridotites and pyroxenites. *Contributions to Mineralogy and Petrology*, **159**, 411–427.

O'Reilly S.Y. and Griffin W.L. (2013) *Mantle Metasomatism, in: Metasomatism and the Chemical Transformation of Rock*. Lecture Notes in Earth System Sciences. Springer Berlin Heidelberg, Berlin, Heidelberg, 471–533, doi: https://doi.org/10.1007/978-3-642-28394-9_12.

Oriolo S. and Becker T. (2018) The Kalahari Craton, Southern Africa: From Archean crustal evolution to Gondwana amalgamation. Pp. 133–159 in: *Geology of Southwest Gondwana* (S. Siegesmund, M.A.S. Basei, P. Oyhantçabal and S. Oriolo, editors), doi: https://doi.org/10.1007/978-3-319-68920-3_6.

Paton C., Hellstrom J., Paul B., Woodhead J. and Hergt J. (2011) Iolite: Freeware for the visualisation and processing of mass spectrometric data. *Journal of Analytical Atomic Spectrometry*, **26**, 2508–2518.

Pearson D.G. and Nowell G.M. (2002) The continental lithospheric mantle: characteristics and significance as a mantle reservoir. *Philosophical Transactions of the Royal Society of London. Series A: Mathematical, Physical and Engineering Sciences*, **360**, 2383–2410.

Pearson D.G. and Wittig N. (2008) Formation of Archaean continental lithosphere and its diamonds: the root of the problem. *Journal of the Geological Society, London*, **165**, 895–914.

Powell R., Holland T. and Worley B. (1998) Calculating phase diagrams involving solid solutions via non-linear equations, with examples using THERMOCALC. *Journal of Metamorphic Geology*, **16**, 577–588.

Rebay G., Powell R. and Diener J.F.A. (2010) Calculated phase equilibria for a MORB composition in a P – T range, 450–650 °C and 18–28 kbar: the stability of eclogite. *Journal of Metamorphic Geology*, **28**, 635–645.

Regier M.E., Mišković A., Ickert R.B., Pearson D.G., Stachel T., Stern R.A. and Kopylova M. (2018) An oxygen isotope test for the origin of Archean mantle roots. *Geochemical Persperctives Letters*, **9**, 6–10.

Schmitz M.D., Bowring S.A., De Wit M.J. and Gartz V. (2004) Subduction and terrane collision stabilize the western Kaapvaal craton tectosphere 2.9 billion years ago. *Earth and Planetary Science Letters*, **222**, 363–376.

Schoene B., de Wit M.J. and Bowring S.A. (2008) Mesoarchean assembly and stabilization of the eastern Kaapvaal craton: A structural-thermochronological perspective. *Tectonics*, **27**, TC5010, doi: https://doi.org/10.1029/2008TC002267.

Schweitzer J. and Kröner A. (1985) Geochemistry and petrogenesis of early Proterozoic intracratonic volcanic rocks of the Ventersdorp Supergroup, South Africa. *Chemical Geology*, **51**, 265–288.

Secchiari A., Montanini A., Bosch D., Macera P. and Cluzel D. (2019) Origin of the spinel-pyroxene symplectites in the harzburgites from the New Caledonia Peridotite. *Ofioliti*, **44**, 31–42.

Simon N.S., Irvine G.J., Davies G.R., Pearson D.G. and Carlson R.W. (2003) The origin of garnet and clinopyroxene in 'depleted' Kaapvaal peridotites. *Lithos*, **71**, 289–322.

Simon N.S.C., Carlson R.W., Pearson D.G. and Davies G.R. (2007) The Origin and Evolution of the Kaapvaal Cratonic Lithospheric Mantle. *Journal of Petrology*, **48**, 589–625.

Sleep N.H. (2003) Survival of Archean cratonal lithosphere. *Journal of Geophysical Research*, **108**, 1–29.

Smith D. (1977) The origin and interpretation of spinel-pyroxene clusters in peridotite. *Journal of Geology*, **85**, 476–482.

Stachel T. (2022) *PTEXL - Geothermobarometry of Mantle Rocks*. https://doi.org/10.5683/SP3/IMYNCL.

Stachel T., Aulbach S., Brey G.P., Harris J.W., Leost I., Tappert R. and Viljoen K.S. (2004) The trace element composition of silicate inclusions in diamonds: a review. *Lithos*, **77**, 1–19.

Sudholz Z.J., Green D.H., Yaxley G.M. and Jaques A.L. (2022) Mantle geothermometry: experimental evaluation and recalibration of Fe–Mg geothermometers for garnet-clinopyroxene and garnet-orthopyroxene in peridotite, pyroxenite and eclogite systems. *Contributions to Mineralogy and Petrology*, **177**, 1–19.

Sun C. and Liang Y. (2013) The importance of crystal chemistry on REE partitioning between mantle minerals (garnet, clinopyroxene, orthopyroxene, and olivine) and basaltic melts. *Chemical Geology*, **358**, 23–36.

Sun C. and Liang Y. (2014) An assessment of subsolidus re-equilibration on REE distribution among mantle minerals olivine, orthopyroxene, clinopyroxene, and garnet in peridotites. *Chemical Geology*, **372**, 80–91.

Sun S.S. and McDonough W.F. (1989) Chemical and isotopic systematics of oceanic basalts: implications for mantle composition and processes. *Geological Society, London, Special Publications*, **42**, 313–345.

Tappe S., Smart K., Torsvik T., Massuyeau M. and de Wit M. (2018) Geodynamics of kimberlites on a cooling Earth: Clues to plate tectonic evolution and deep volatile cycles. *Earth and Planetary Science Letters*, **484**, 1–14.

Taylor W.R. (1998) An experimental test of some geothermometer and geobarometer formulations for upper mantle peridotites with application to the thermobarometry of fertile lherzolite and garnet websterite. *Neues Jahrbuchfür Mineralogie, Abhandlungen*, **172**, 381–408.

Tomlinson E.L. and Holland T.J.B. (2021) A thermodynamic model for the subsolidus evolution and melting of peridotite. *Journal of Petrology*, **62**, egab012, https://doi.org/10.1093/petrology/egab012.

Tomlinson E.L. and Kamber B.S. (2021). Depth-dependent peridotite-melt interaction and the origin of variable silica in the cratonic mantle. *Nature Communications*, **12**, 1082.

Tomlinson E.L., Kamber B.S., Hoare B.C., Stead C.V. and Ildefonse B. (2018) An exsolution origin for Archean mantle garnet. *Geology*, **46**, 123–126.

Walter M.J. (1998) Melting of Garnet Peridotite and the Origin of Komatiite and Depleted Lithosphere. *Journal of Petrology*, **39**, 29–60.

Wang H., van Hunen J. and Pearson G. (2018) Making Archean cratonic roots by lateral compression: A two-stage thickening and stabilization model. *Tectonophysics*, **746**, 562–571.

Wasch L.J., Van Der Zwan F.M., Nebel O., Morel M.L.A., Hellebrand E.W.G., Pearson D.G. and Davies G.R. (2009) An alternative model for silica enrichment in the Kaapvaal subcontinental lithospheric mantle. *Geochimica et Cosmochimica Acta*, **73**, 6894–6917.

Ziberna L., Nimis P., Kuzmin D. and Malkovets V.G. (2016) Error sources in single-clinopyroxene thermobarometry and a mantle geotherm for the Novinka kimberlite. Yakutia. *American Mineralogist*, **101**, 2222–2232.